

ODIN: Confirmation and 3D Reconstruction of Six Massive Protoclusters at Cosmic Noon

ASHLEY ORTIZ,¹ VANDANA RAMAKRISHNAN,¹ KYOUNG-SOO LEE,¹ ARJUN DEY,² YUCHENG GUO,³ ETHAN PINARSKI,¹
ANAND RAICHOOR,⁴ FRANCISCO VALDES,² J. AGUILAR,⁴ S. AHLEN,⁵ MARIA CELESTE ARTALE,⁶ D. BIANCHI,^{7,8}
AUGUST BLIESE,¹ D. BROOKS,⁹ R. CANNING,¹⁰ MARIA CANDELA CERDOSINO,^{11,12} T. CLAYBAUGH,⁴ A. CUCEU,⁴
A. DE LA MACORRA,¹³ P. DOEL,⁹ J. E. FORERO-ROMERO,^{14,15} ERIC GAWISER,¹⁶ E. GAZTAÑAGA,^{17,10,18}
S. GONTCHO A GONTCHO,¹⁹ CARYL GRONWALL,^{20,21} LUCIA GUAITA,^{6,22} G. GUTIERREZ,²³ H. K. HERRERA-ALCANTAR,^{24,25}
HO SEONG HWANG,^{26,27} WOONG-SEOB JEONG,²⁸ R. JOYCE,² R. KEHOE,²⁹ T. KISNER,⁴ A. KREMIN,⁴ ANKIT KUMAR,³⁰
O. LAHAV,⁹ M. LANDRIAU,⁴ JAEHYUN LEE,³¹ SEONG-KOOK LEE,²⁶ L. LE GUILLOU,³² M. MANERA,^{33,34} A. MEISNER,²
R. MIQUEL,^{35,34} BYEONGHA MOON,²⁸ J. MOUSTAKAS,³⁶ A. D. MYERS,³⁷ S. NADATHUR,¹⁰ N. PALANQUE-DELABROUILLE,^{25,4}
CHANGBOM PARK,³⁸ W. J. PERCIVAL,^{39,40,41} I. PÉREZ-RÀFOLS,⁴² F. PRADA,⁴³ ESHWAR PUVVADA,¹ G. ROSSI,⁴⁴
E. SANCHEZ,⁴⁵ D. SCHLEGEL,⁴ M. SCHUBNELL,^{46,47} J. SILBER,⁴ HYUNMI SONG,⁴⁸ D. SPRAYBERRY,² G. TARLÉ,⁴⁷
PAULINA TRONCOSO IRIBARREN,⁴⁹ ANA SOFÍA M. UZSOY,⁵⁰ B. A. WEAVER,² YUJIN YANG,²⁸ R. ZHOU,⁴ AND H. ZOU⁵¹

¹Department of Physics and Astronomy, Purdue University, 525 Northwestern Ave., West Lafayette, IN 47906, USA

²NSF NOIRLab, 950 N. Cherry Ave., Tucson, AZ 85719, USA

³School of Earth and Space Exploration, Arizona State University, Tempe, AZ 85287, USA

⁴Lawrence Berkeley National Laboratory, 1 Cyclotron Road, Berkeley, CA 94720, USA

⁵Department of Physics, Boston University, 590 Commonwealth Avenue, Boston, MA 02215 USA

⁶Universidad Andres Bello, Facultad de Ciencias Exactas, Departamento de Física y Astronomía, Instituto de Astrofísica, Fernandez Concha 700, Las Condes, Santiago RM, Chile

⁷Dipartimento di Fisica “Aldo Pontremoli”, Università degli Studi di Milano, Via Celoria 16, I-20133 Milano, Italy

⁸INAF-Osservatorio Astronomico di Brera, Via Brera 28, 20122 Milano, Italy

⁹Department of Physics & Astronomy, University College London, Gower Street, London, WC1E 6BT, UK

¹⁰Institute of Cosmology and Gravitation, University of Portsmouth, Dennis Sciama Building, Portsmouth, PO1 3FX, UK

¹¹Instituto de Astronomía Teórica y Experimental (IATE), CONICET-UNC, Laprida 854, X500BGR, Córdoba, Argentina

¹²Facultad de Matemática, Astronomía, Física y Computación, Universidad Nacional de Córdoba (FaMAF-UNC), Bvd. Medina Allende s/n, Ciudad Universitaria, X5000HUA, Córdoba, Argentina

¹³Instituto de Física, Universidad Nacional Autónoma de México, Circuito de la Investigación Científica, Ciudad Universitaria, Cd. de México C. P. 04510, México

¹⁴Departamento de Física, Universidad de los Andes, Cra. 1 No. 18A-10, Edificio Ip, CP 111711, Bogotá, Colombia

¹⁵Observatorio Astronómico, Universidad de los Andes, Cra. 1 No. 18A-10, Edificio H, CP 111711 Bogotá, Colombia

¹⁶Department of Physics and Astronomy, Rutgers, the State University of New Jersey, Piscataway, NJ 08854, USA

¹⁷Institut d’Estudis Espacials de Catalunya (IEEC), c/ Esteve Terradas 1, Edifici RDIT, Campus PMT-UPC, 08860 Castelldefels, Spain

¹⁸Institute of Space Sciences, ICE-CSIC, Campus UAB, Carrer de Can Magrans s/n, 08913 Bellaterra, Barcelona, Spain

¹⁹University of Virginia, Department of Astronomy, Charlottesville, VA 22904, USA

²⁰Institute for Gravitation and the Cosmos, The Pennsylvania State University, University Park, PA 16802, USA

²¹Department of Astronomy & Astrophysics, The Pennsylvania State University, University Park, PA 16802, USA

²²Millennium Nucleus for Galaxies (MINGAL)

²³Fermi National Accelerator Laboratory, PO Box 500, Batavia, IL 60510, USA

²⁴Institut d’Astrophysique de Paris. 98 bis boulevard Arago. 75014 Paris, France

²⁵IRFU, CEA, Université Paris-Saclay, F-91191 Gif-sur-Yvette, France

²⁶SNU Astronomy Research Center, Seoul National University, 1 Gwanak-ro, Gwanak-gu, Seoul 08826, Republic of Korea

²⁷Astronomy Program, Department of Physics and Astronomy, Seoul National University, 1 Gwanak-ro, Gwanak-gu, Seoul 08826, Republic of Korea

²⁸Korea Astronomy and Space Science Institute, 776 Daedeokdae-ro, Yuseong-gu, Daejeon 34055, Republic of Korea

²⁹Department of Physics, Southern Methodist University, 3215 Daniel Avenue, Dallas, TX 75275, USA

³⁰Departamento de Ciencias Físicas, Universidad Andres Bello, Fernandez Concha 700, Las Condes, Santiago, Chile

³¹Korea Astronomy and Space Science Institute, 776, Daedeokdae-ro, Yuseong-gu, Daejeon 34055, Republic of Korea

³²Sorbonne Université, CNRS/IN2P3, Laboratoire de Physique Nucléaire et de Hautes Energies (LPNHE), FR-75005 Paris, France

³³Departament de Física, Serra Húnter, Universitat Autònoma de Barcelona, 08193 Bellaterra (Barcelona), Spain

³⁴Institut de Física d’Altes Energies (IFAE), The Barcelona Institute of Science and Technology, Edifici Cn, Campus UAB, 08193, Bellaterra (Barcelona), Spain

³⁵Institució Catalana de Recerca i Estudis Avançats, Passeig de Lluís Companys, 23, 08010 Barcelona, Spain

³⁶Department of Physics and Astronomy, Siena University, 515 Loudon Road, Loudonville, NY 12211, USA

³⁷Department of Physics & Astronomy, University of Wyoming, 1000 E. University, Dept. 3905, Laramie, WY 82071, USA

³⁸*Korea Institute for Advanced Study, 85 Hoegi-ro, Dongdaemun-gu, Seoul 02455, Republic of Korea*

³⁹*Department of Physics and Astronomy, University of Waterloo, 200 University Ave W, Waterloo, ON N2L 3G1, Canada*

⁴⁰*Perimeter Institute for Theoretical Physics, 31 Caroline St. North, Waterloo, ON N2L 2Y5, Canada*

⁴¹*Waterloo Centre for Astrophysics, University of Waterloo, 200 University Ave W, Waterloo, ON N2L 3G1, Canada*

⁴²*Departament de Física, EEBE, Universitat Politècnica de Catalunya, c/Eduard Maristany 10, 08930 Barcelona, Spain*

⁴³*Instituto de Astrofísica de Andalucía (CSIC), Glorieta de la Astronomía, s/n, E-18008 Granada, Spain*

⁴⁴*Department of Physics and Astronomy, Sejong University, 209 Neungdong-ro, Gwangjin-gu, Seoul 05006, Republic of Korea*

⁴⁵*CIEMAT, Avenida Complutense 40, E-28040 Madrid, Spain*

⁴⁶*Department of Physics, University of Michigan, 450 Church Street, Ann Arbor, MI 48109, USA*

⁴⁷*University of Michigan, 500 S. State Street, Ann Arbor, MI 48109, USA*

⁴⁸*Department of Astronomy and Space Science, Chungnam National University, 99 Daehak-ro, Yuseong-gu, Daejeon, 34134, Republic of Korea*

⁴⁹*Facultad de Ingeniería y Arquitectura, Universidad Central de Chile, Avenida Francisco de Aguirre 0405, 171-0614 La Serena, Coquimbo, Chile*

⁵⁰*Center for Astrophysics | Harvard & Smithsonian, 60 Garden St., Cambridge, MA 02138, USA*

⁵¹*National Astronomical Observatories, Chinese Academy of Sciences, A20 Datun Road, Chaoyang District, Beijing, 100101, P. R. China*

ABSTRACT

Protoclusters represent sites of accelerated galaxy formation and extreme astrophysical activity characteristic of dense environments. Identifying massive protoclusters and mapping their spatial structures are therefore crucial first steps in understanding how the large-scale environment influences galaxy evolution. We combine wide-field Ly α imaging from the ODIN survey with extensive DESI and ancillary spectroscopy across the extended COSMOS and XMM-LSS fields (≈ 14 deg²) to search for massive protoclusters. We confirm six systems at $z \approx 2.4$ and $z \approx 3.1$, reconstruct their three-dimensional structures, estimate descendant halo masses, and, for one structure at $z \approx 3.12$, demonstrate that overlapping narrowband filters (*NB497* and *N501*) provide accurate redshift tomography for emission-line galaxies. One protocluster at $z \approx 2.45$ overlaps with one of the LATIS tomographic fields, enabling direct comparison between galaxy and H I overdensities traced by Ly α forest absorption. Another at $z \approx 3.12$ hosts a massive quiescent galaxy ($M_* \approx 1.2 \times 10^{11} M_\odot$), indicating early quenching in a dense environment. By comparing Ly α emission properties across environments, we find that protocluster galaxies exhibit higher median line fluxes and a deficit of faint emitters relative to the field. The effect is strongest when both 2D and 3D density information are combined, indicating that galaxies in the densest protocluster cores are most affected by environmental processes. This effect is stronger at $z \approx 3.1$ than at $z \approx 2.4$, suggesting possible redshift evolution.

1. INTRODUCTION

Clusters of galaxies are the most massive gravitationally bound objects in the Universe. At high redshift ($z \gtrsim 2$), the progenitors of galaxy clusters, or *protoclusters*, host copious star formation and AGN activity (e.g., Casey et al. 2015; Umehata et al. 2015; Oteo et al. 2018), potentially in excess of the field (e.g., Lemaux et al. 2022; Popescu et al. 2023). Simulations suggest that the formation of galaxies is accelerated within overdense environments (Chiang et al. 2017; Muldrew et al. 2018), supported by observations of massive and evolved galaxies in these regions (e.g., Ito et al. 2023; Jin et al. 2024). Yet, the specific physical processes driving this accelerated evolution remain unclear.

The One-hundred-deg² DECam Imaging in Narrowbands (ODIN: Lee et al. 2024) survey has made progress towards understanding the mechanisms at play in overdense environments, by identifying a statistical sample

of ~ 150 protoclusters at Cosmic Noon (Ramakrishnan et al. 2024, 2025a). These protoclusters are identified within narrow cosmic slices ($\Delta z \sim 0.06 - 0.08$) as overdensities of Ly α emitting galaxies (LAEs). Analysis of their halo bias suggests that the ODIN protoclusters correspond to halos with masses of $\sim 10^{13-13.5} M_\odot$ at the time of observation, evolving into clusters with mass $\gtrsim 10^{14.5} M_\odot$ by $z = 0$ (Ramakrishnan et al. 2025a).

In order to establish the processes affecting galaxies in protoclusters, we must first accurately place these galaxies within the structure. The typical size of a protocluster is $\approx 5 - 10$ cMpc (Chiang et al. 2013); identifying the regions corresponding to the protocluster core, outskirts, and connected cosmic filaments thus requires mapping these regions in three dimensions with an accuracy of $\sim 2 - 3$ cMpc or better.

Recently, in Ramakrishnan et al. (2025b), we presented a method to trace the 3D structures of proto-

clusters on scales of ≈ 50 cMpc, capturing both the most overdense peaks and the less-dense regions connecting them. This method combined LAEs photometrically selected from ODIN narrowband imaging with a subset of spectroscopically confirmed LAEs to maximize the recovery of the large-scale structure (LSS). By constructing 3D maps of two massive structures at $z \approx 3.1$, we demonstrated that extended and luminous Ly α nebulae or ‘blobs’ (LABs) preferentially reside at the *outskirts* of the most overdense environments. This trend was obscured by the effects of projection in 2D, highlighting the importance of a 3D perspective.

In this work, we extend the method of Ramakrishnan et al. (2025b) to six protocluster systems identified by ODIN, located in the COSMOS and XMM-LSS fields at $z \approx 2.4$ and 3.1. These systems were identified as significant LAE overdensities from the ODIN surface density maps and have extensive spectroscopic data available from the Dark Energy Spectroscopic Instrument (DESI). We combine the LAEs spectroscopically confirmed by DESI with the full sample of photometrically selected ODIN LAEs to trace the 3D morphology of these structures and estimate their descendant mass. We further identify a sample of ~ 250 LAEs which are confirmed to lie within these protoclusters and utilize them to investigate the effects of environment on the observed Ly α emission.

The structure of this paper is as follows: in Section 2, we describe the imaging and spectroscopy data, along with the selection criteria for LAEs, LABs, and protoclusters used in the analyses. In Section 3, we explain the approach used to estimate redshift through filter tomography and validate these results against spectroscopic redshifts within a section of one of the fields in this study. Section 4 covers the 3D detection and characterization of ODIN protoclusters, and it is followed by an in-depth discussion of the six protoclusters identified using this method, in light of existing literature, in Section 5. In Section 6, we calculate the line flux of all confirmed LAEs and examine their variation across different environments. Lastly, Section 7 recaps our primary findings. We adopt a Λ CDM concordance cosmology with parameters $h = 0.7$, $\Omega_m = 0.27$, and $\Omega_\Lambda = 0.73$ and use comoving distance scales unless noted otherwise.

2. DATA

This study uses both photometric and spectroscopic samples of LAEs identified in the extended COSMOS and XMM-LSS fields, covering a total sky area of ≈ 14 deg 2 . The imaging data are taken as part of the

ODIN survey (Lee et al. 2024), which covers ≈ 90 deg 2 in total. The selection procedures of LAEs and protoclusters, as well as spectroscopic observations, are presented in detail elsewhere (Firestone et al. 2024; Pinarski et al. 2026; Dey et al. in prep). Here, we only provide a summary of the relevant datasets. Table 1 lists the LAE-, LAB-, and protocluster samples we utilize in this work.

2.1. Samples of LAEs, LABs, and Protoclusters

The LAEs were initially selected based on their narrow-to-broad-band flux excess in either the $N419$ or $N501$ filters, corresponding to redshifts of $z \approx 2.4$ and $z \approx 3.1$, respectively. Both filters have a full width at half maximum (FWHM) of 70–75 Å, which defines a redshift slice of $\Delta z \approx 0.06$ across each filter. A full description of the ODIN LAE photometric selection method is provided in Firestone et al. (2024). The resulting photometric LAE counts are 6,441 ($z \approx 2.4$) and 6,069 ($z \approx 3.1$) in the COSMOS field, and 5,728 ($z \approx 2.4$) and 3,991 ($z \approx 3.1$) in the XMM-LSS field. Follow-up spectroscopy indicates that contamination¹ from low-redshift interlopers is minimal—less than 4% for $z \approx 3.1$ and 6% for $z \approx 2.4$ (Pinarski et al. 2026). These interlopers are roughly uniformly distributed and primarily act as a background population. As a result, they may slightly reduce the contrast of measured overdensities but do not generate artificial structures or significantly bias the identification of protoclusters.

It is challenging to compare the contamination rate of the ODIN LAE samples with those reported in existing studies (e.g., Sobral et al. 2018), as it depends on the equivalent width cut and line flux limits, among other factors. The details of the interloper fraction as a function of NB brightness are presented in Pinarski et al. (2026).

We also utilize the LABs identified from the ODIN survey data. The selection method of LABs is presented in Moon et al. (2025). While similar in principle to the LAE selection, it further requires a flux-dependent minimum size threshold, effectively isolating true extended sources. 112 (47) and 103 (25) LABs are found in COSMOS (XMM-LSS) at $z \approx 2.4$ and 3.1, respectively. The first clustering analysis of ODIN LABs suggests that cosmic variance is non-negligible even in a relatively large survey area (> 6 deg 2 ; Moon et al. 2026).

Given the narrow bandwidths of the ODIN filters, protocluster candidates are first identified as regions with elevated LAE surface densities, since contamination

¹ The contamination fraction is defined here as the number of confirmed interlopers divided by the total number of sources that yielded secure spectroscopic redshifts.

Table 1. Summary of object samples

Field/Filter	Redshift	Effective area [deg ²]	N_{LAE}^a	N_{spec}^b	N_{LAB}^c	N_{PC}^d
COSMOS/ <i>N</i> 419	2.419–2.480	7.3	6,441	1,916	103	28
XMM-LSS/ <i>N</i> 419	2.419–2.480	6.6	5,728	1,161	47	36
COSMOS/ <i>N</i> 501	3.093–3.155	7.3	6,069	1,418	112	41
XMM-LSS/ <i>N</i> 501	3.093–3.155	6.6	3,991	154 ^e	25	35
Total		13.9	22,229	4,649	287	140

^aNumber of photometrically selected LAEs (Firestone et al. 2024)

^bNumber of LAEs with redshift information (Pinarski et al. 2026)

^cNumber of photometrically selected LABs (Moon et al. 2025)

^dNumber of 2D protocluster candidates (Ramakrishnan et al. 2024)

^eIncluding spectroscopically confirmed LAEs and those with redshifts from dual-narrowband tomography (see Section 3)

from foreground and background galaxies is expected to be minimal. The photometric (i.e., two-dimensional) protocluster selection method used by ODIN is described in detail in Ramakrishnan et al. (2024). The sky positions and angular extent of the individual 2D protocluster candidates are shown in Figure 1 as yellow contours. As discussed in Section 4, our three-dimensional reconstruction detects protoclusters in full spatial context. Notably, all of the protocluster structures analyzed in this study (indicated by red boxes in Figure 1) correspond to one or more of these 2D-selected protoclusters.

2.2. DESI-ODIN Spectroscopy

DESI is a wide-field, fiber-fed spectrograph mounted on the Mayall 4m telescope at Kitt Peak National Observatory (DESI Collaboration et al. 2022). The instrument is currently carrying out a spectroscopic survey covering $\sim 17,000$ deg² of the sky (Schlafly et al. 2023; DESI Collaboration et al. 2025) to place constraints on the nature of dark energy (Adame et al. 2025; Abdul Karim et al. 2025).

Based on the ODIN narrowband imaging, DESI obtained spectroscopic observations of a subset of photometric LAEs selected using less restrictive criteria than the ODIN LAEs. DESI is capable of obtaining spectra of up to ~ 5000 sources per pointing (DESI Collaboration et al. 2016; Miller et al. 2024; Poppett et al. 2024), and as a result the DESI-ODIN observations covered a total of 11,599 targets, of which 7,973 yielded reliable classifications. The redshifts of these sources were determined via visual inspection (Pinarski et al. 2026) of

the spectra reduced via the DESI pipeline (Guy et al. 2023).

Less than half of the DESI targets are formally selected as ODIN LAEs. However, a closer examination showed that a large fraction of the former were simply removed from the ODIN selection because they lie within the conservative star masks, are located outside of the deep broadband data ODIN uses, or have slightly smaller narrowband excesses than those adopted by ODIN (Pinarski et al. 2026). Unlike the ODIN LAE selection, which uses broadband data from the Subaru Strategic Program Deep fields (Aihara et al. 2019), the DESI target selection also used the shallower broadband data from the Legacy Survey to fully utilize the DESI field of view. Details of the DESI target selection will be presented in a future paper (Dey et al. in prep).

Given that there is no fundamental difference between DESI-confirmed galaxies at $z \approx 2.4$ and 3.1 that are in and outside the ODIN LAE samples, we choose to utilize all DESI-confirmed LAEs classified with the spectral type² of galaxy and quality flag³ $q \geq 2.5$, which lie at the intended redshift range. Both quantities are determined as part of the visual inspection campaign (Pinarski et al. 2026; Dey et al. in prep), with redshifts

² Any source exhibiting broad lines of any kind or narrow lines typically absent in star-forming galaxies – such as He II, or C III] – is classified with the spectral type AGN.

³ According to the classification scheme, $q=3$ means one prominent feature is detected while $q=2$ means possible but uncertain spectral feature is detected. The final quality flag is averaged over individual evaluations.

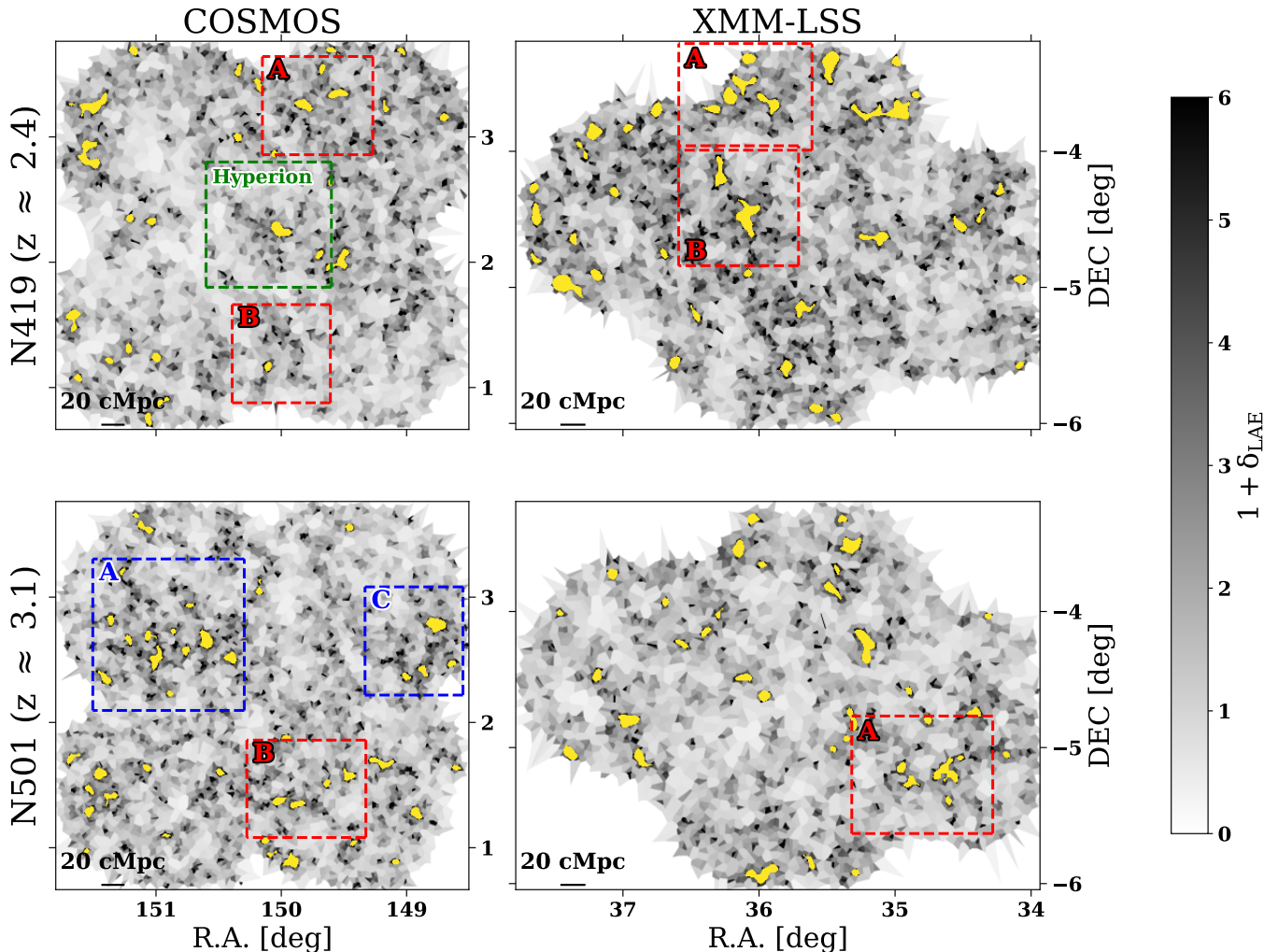


Figure 1. Protocluster candidates in COSMOS and XMM-LSS fields (yellow swatches) with the areas we consider in this work highlighted by red boxes. The greyscale background indicates the surface density of photometrically selected LAEs, with darker colors corresponding to higher values, as indicated by the colorbar. The structures considered in Ramakrishnan et al. (2025b) are marked in blue while a confirmed proto-super-cluster, *Hyperion* (Cucciati et al. 2018) is marked in green.

defined by the Ly α emission-line peak and no correction to systemic redshifts applied. The number of spec- z sources satisfying these criteria and subsequently used in this study is 1,916 ($z \approx 2.4$) and 1,418 ($z \approx 3.1$) in the COSMOS field and 1,161 ($z \approx 2.4$) in the XMM-LSS field, respectively. No $z \approx 3.1$ LAE targets were observed in XMM-LSS with DESI (but see Section 3 for further details). Although AGN host galaxies can also reside in protocluster environments at our redshift range, we exclude objects classified as AGN to maintain consistency with our later analysis of Ly α luminosity versus environment in Section 6. The number of AGN in our DESI sample at the intended redshift range is small (< 50), so their inclusion would not affect our protocluster selection in any case (see also Pinarski et al. 2026).

We note that, while additional targeted spectroscopy has been obtained in these fields using the Keck and Gemini telescopes, those observations are concentrated primarily on the two protocluster complexes analyzed by Ramakrishnan et al. (2025b), indicated by the blue boxes in Figure 1. We do not include these data in our analysis because their depth and targeted sampling strategy differ substantially from the uniform DESI-ODIN spectroscopic selection. For a detailed discussion of these two complexes and the associated follow-up spectroscopy, we refer the reader to Ramakrishnan et al. (2025b).

3. ESTIMATING REDSHIFTS WITH TWO OVERLAPPING NARROWBAND FILTERS

While DESI spectroscopic coverage does not extend to N501 LAEs in the XMM-LSS field, a $\approx 0.7 \text{ deg}^2$ sub-

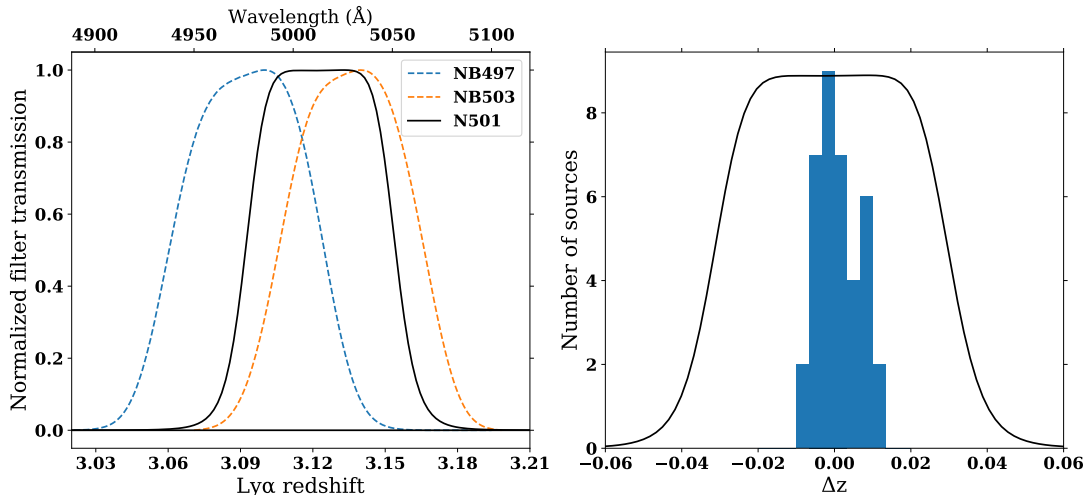


Figure 2. *Left:* *NB497* and *NB503* filters of *G20*, shown in comparison to the ODIN *N501* filter. The three filters have significant overlap. *Right:* the offset between spectroscopic and tomographic redshifts, $\Delta z = z_{\text{spec}} - z_{\text{tomog}}$, is plotted together with the *N501* transmission. The median value of offset is 0 and its standard deviation is 0.005, an order of magnitude smaller than the FWHM of the *N501* filter.

section of the field (corresponding to the SXDS field, [Furusawa et al. 2008](#)) was imaged with two narrowband filters, *NB497* and *NB503* ($\lambda_C = 4986 \text{ \AA}$ and 5030 \AA ; FWHM $\Delta\lambda = 78 \text{ \AA}$ and 74 \AA , respectively; [Guo et al. 2020](#)). As illustrated in the left panel of Figure 2, these filters are similar in width and overlap with *N501*.

By combining these narrowband observations with broadband data, [Guo et al. \(2020, hereafter G20\)](#) defined LAE samples based on the *NB497* and *NB503* flux excess. A subset of those LAEs were followed up with MMT Hectospec observations, yielding 166 unique source redshifts. These include about 30 confirmed galaxies in and around a significant overdensity of *NB497* LAEs at $z \approx 3.09$ (see their Figure 1). The same region is identified as a high overdensity of *N501* LAEs by the ODIN survey.

We cross-match our *N501* ODIN LAE catalog against the list of spectroscopically confirmed LAEs from *G20* (see their Table 2), finding 90 matches. Taking advantage of the availability of a large spectroscopic sample and the substantial overlap between *NB497* and *N501*, we apply the methodology presented in [Zabl et al. \(2016\)](#), referred to as *narrowband tomography*, to estimate redshifts of additional sources in this overdense structure. We do not use *NB503* for the subsequent analysis as it overlaps too much with *N501* to be useful for tomographic purposes.

The observed flux density of a Ly α emitting galaxy⁴ at redshift z observed with a narrowband filter is:

$$f_{\nu, \text{NB}} = \frac{\int \lambda f_{\lambda}(\lambda) \mathcal{R}(\lambda) d\lambda}{\int c \mathcal{R}(\lambda) \lambda^{-1} d\lambda} \quad (1)$$

where $f_{\lambda}(\lambda)$ is the underlying spectral energy distribution of the galaxy at wavelength λ (in units of $\text{erg s}^{-1} \text{ cm}^{-2} \text{ \AA}^{-1}$), $\mathcal{R}(\lambda)$ is the filter transmission, and c is the speed of light (in units of cm s^{-1}). We make a simplifying assumption that the flux sampled by the filter is dominated by the emission line. Additionally, we assume that the line profile can be reasonably approximated by a Dirac delta function: i.e., $f_{\lambda}(\lambda) \approx f_{\text{Ly}\alpha} \delta(\lambda - \lambda_0)$, where $\lambda_0 = 1215.67(1+z) \text{ \AA}$. In this case, Equation 1 is reduced to $f_{\nu, \text{NB}} \approx F_{\text{Ly}\alpha} \mathcal{R}(\lambda_0) / \mathcal{C}$, where $F_{\text{Ly}\alpha} = \lambda_0 f_{\text{Ly}\alpha}$ is the total flux of the Ly α line and \mathcal{C} is a filter-dependent constant. This is justified because the intrinsic Ly α line widths (FWHM $\sim 3 - 6 \text{ \AA}$) of LAEs are extremely narrow compared to the width of our narrowband filters ([Erb et al. 2014](#); [Blaziot et al. 2023](#)).

If the Ly α line falls into two adjacent narrowbands (say 1 and 2), the simplified Equation 1 can be written for each filter as:

$$\begin{aligned} f_{\nu, 1} &= F_{\text{Ly}\alpha} \mathcal{R}_1(\lambda_0) / \mathcal{C}_1 \\ f_{\nu, 2} &= F_{\text{Ly}\alpha} \mathcal{R}_2(\lambda_0) / \mathcal{C}_2 \end{aligned} \quad (2)$$

where \mathcal{R}_1 and \mathcal{R}_2 are the transmissions of filter 1 and 2 and \mathcal{C}_1 and \mathcal{C}_2 are the integrals over these transmission

⁴ While the line is assumed to be Ly α , we note that the methodology can be applied to any strong line.

functions. As the same line is sampled by two different filters modulated by their respective transmission curves, it has a different apparent brightness in each filter. Provided that the filter transmissions are accurately measured, solving these two equations simultaneously determines the redshift of the source.

We utilize this method on 36 spectroscopic sources for which $NB497$ and $N501$ fluxes have been recorded. In the right panel of Figure 2, $\Delta z \equiv z_{\text{spec}} - z_{\text{tomog}}$ is depicted, where z_{tomog} represents the tomographic redshift estimate. The median shift is 0, with a standard deviation of $\sigma(\Delta z) = 0.005$, which is over ten times smaller than the FWHM of either filter. The dispersion equates to $\lesssim 1.2$ pMpc or 4.8 cMpc along the line-of-sight. Despite this uncertainty being greater than that of spectroscopic redshifts, it remains smaller than the average protocluster size (e.g., Chiang et al. 2013). Therefore, tomographic redshifts could be advantageous in analyzing the spatial structure of protoclusters and their environment. Using this methodology, we acquire redshift estimates for an additional 64 ODIN LAEs that lack spectroscopic validation. These redshift estimates are used together with spectroscopic redshifts in 3D detection and reconstruction of ODIN protoclusters outlined in the next section.

4. CHARACTERIZING SPATIAL STRUCTURES OF PROTOCLUSTERS

4.1. Probabilistic 3D Reconstruction

A comprehensive description of our probabilistic reconstruction technique is given in Ramakrishnan et al. (2025b, Section 3.1), along with thorough validation using cosmological hydrodynamic simulations processed to emulate the ODIN data (refer also to, Ramakrishnan et al. 2024). In this section, we provide a summary. Our method relies on the premise that spectroscopic redshifts from a randomly chosen subset of the base sample can adequately represent the overall distribution within a particular sightline. Although this premise might not always hold in average or low-density areas, it is likely applicable in high-density protocluster sightlines. Based on this premise, we utilize all LAEs with measured redshifts (spectroscopic and tomographic) to create sightline-dependent redshift priors, which are then used to statistically assign redshifts to ODIN LAEs lacking direct redshift measurements.

We proceed as follows. First, we divide each protocluster volume into a three-dimensional grid with 2 cMpc spacing, equivalent to $60''$ – $70''$ in the transverse direction and $\Delta z \approx 0.002$ along the line of sight. Spec-z LAEs are binned into this grid, and their distribution is smoothed using a 3D Gaussian kernel with FWHM 5–

7 cMpc, to minimize shot noise while preserving spatial characteristics. A small constant is added to each bin to prevent zero-probability regions. This smoothed histogram serves as a redshift prior for each sightline. Second, by drawing from these priors, we assign redshifts for unconfirmed LAEs. In cases where no spectroscopic data is available in a given sightline, the redshift prior is assumed to be that inferred from the NB filter transmission. This process is repeated and averaged over 500 realizations, resulting in a statistically reliable 3D density field of LAEs, to map the underlying large-scale structure at a 2 cMpc resolution.

In Ramakrishnan et al. (2025b), we found that reconstructed 3D maps produced as described above give a reasonable approximation to the underlying dark matter distribution, consistently outperforming that constructed solely based on spectroscopic sources. We further showed in that work (Appendix B therein) that the peculiar motion of galaxies has minimal effect on our 3D reconstructions, which we attribute to the fact that the uncertainty in the line-of-sight position arising from such motion ($\sim 2.5 - 4$ cMpc) is much smaller than the typical size of a protocluster ($\sim 10 - 20$ cMpc). Similarly, the 3D reconstructions are not significantly affected by the uncertainty in the redshift estimates obtained via narrowband tomography, as we discuss in the following section. Unsurprisingly, the main limitation is set by the spectroscopic sampling fraction (f_{spec}): i.e., the fraction of sources with spectroscopic coverage. Since these sources serve as our priors, a higher f_{spec} enables a more accurate recovery of the underlying dark matter distribution. Increasing f_{spec} from 0.2 to 1 improved the reconstruction accuracy by up to 25%. The typical f_{spec} across our fields is $\sim 0.2 - 0.4$.

4.2. The Impact of Redshift Uncertainty on 3D Reconstruction

The redshift information used in the 3D reconstruction is subject to several sources of uncertainty. Spectroscopic redshifts are primarily based on the peak of Ly α emission, which is known to be offset from the systemic velocity (by 150–200 km s $^{-1}$, with some scatter; e.g., Hashimoto et al. 2013) due to radiative transfer effects. Even when systemic redshifts can be accurately measured, peculiar motion due to local gravity can shift them from true cosmological redshifts by 200–300 km s $^{-1}$. In addition, the tomographic redshifts derived in Section 3 generally have larger uncertainties ($\sigma_z=0.005$) than the spectroscopic redshifts.

In Appendix B of Ramakrishnan et al. (2025b), we quantified how the radiative transfer effects and peculiar motion may influence the 3D reconstruction, using

the IllustrisTNG300-1 simulation suite (Pillepich et al. 2018a,b; Nelson et al. 2019). In a $(60 \text{ cMpc})^3$ volume centered on the $z = 3$ progenitors of massive clusters, we populate a sample of mock LAEs with the number density matched to the real data. A fraction of these sources are designated as the ‘spectroscopic sources’; their cosmological redshifts are then perturbed accordingly to match these systematic effects. The remainder are treated as the photometric LAE sample. The 3D reconstruction procedure is then conducted in an identical manner to the real data, as described in Section 4.1.

The resultant 3D model is then compared with the dark matter distribution using a metric called total variation distance (TVD; Tsybakov 2009), measuring the similarity of two probability distributions. The TVD ranges from 0 for identical distributions to 1 for completely distinct distributions. We found that the difference in TVD value with or without these effects is smaller than the scatter among different realizations (see Figure 15 of Ramakrishnan et al. 2025b).

In this work, we carry out a similar test to check the robustness of 3D reconstruction using tomographic redshifts. This time, we perturb the redshifts by drawing new values from a normal distribution centered on the true redshift and with a standard deviation of $\sigma_z = 0.005$ (see Figure 2). We find that the reconstruction using the ‘perturbed’ redshifts has a similar TVD to that using the ‘true’ redshifts with a typical difference of $\lesssim 5\%$, indicating that larger uncertainties from tomographic redshifts do not significantly affect our 3D reconstructions.

4.3. Detection and Descendant Mass estimates of Protoclusters

From the reconstructed maps presented in Section 4.1, we identify protoclusters as contiguous regions where the three-dimensional density field reaches or exceeds the 97th percentile within a given field and encloses a volume greater than 500 cMpc^3 . The resulting enclosed volume is defined as the protocluster volume, V_{PC} . The minimum volume threshold of 500 cMpc^3 is roughly equivalent to a sphere of radius 5 cMpc and is consistent with the effective line-of-sight resolution set by the $z_{\text{spec}} - z_{\text{tom}}$ scatter (4.8 cMpc). The 97th percentile density threshold was calibrated using IllustrisTNG mock catalogs (Ramakrishnan et al. 2025b, Section 6.2), which showed that regions above this percentile most reliably correspond to the progenitors of massive $z = 0$ halos and yield descendant-mass esti-

mates with a scatter of only 0.2–0.3 dex relative to their true values.

Descendant masses, $M_{\text{est}}^{z=0}$, are then estimated as the total mass within V_{PC} as (Steidel et al. 1998, 2000):

$$M_{\text{est}}^{z=0} = \left(1 + \frac{\delta_g}{b_g}\right) \rho_0 V_{\text{PC}} \quad (3)$$

where ρ_0 is the mean comoving cosmic density, δ_g is the mean 3D galaxy overdensity within the protocluster volume, and b_g is the galaxy bias. The latter two are related to matter overdensity, δ_m , as: $\delta_g = b_g \delta_m$. Clustering measurements of ODIN LAEs give $b_g = 1.7 \pm 0.2$ and $b_g = 2.0 \pm 0.2$ at $z \approx 2.4$ and $z \approx 3.1$ (White et al. 2024; Herrera et al. 2025). Since our analysis includes both redshifts, we could, in principle, adopt distinct bias values at each redshift; however, the difference between the two is small. Varying b_g within this range changes the inferred descendant masses only minimally: using $b_g = 1.8$ instead of the upper-end value $b_g = 2.2$ modifies $\log_{10}(M_{\text{est}}^{z=0})$ by $\lesssim 0.07$ dex, far below our overall uncertainty of 0.2–0.3 dex. For this reason, we adopt a single representative value $b_g = 1.8$.

Within the surveyed area of 14 deg^2 , the DESI spectroscopy provided a relatively sparse sampling of our photometric LAEs. Furthermore, the fiber-assignment algorithm leads to non-uniform coverage, meaning some regions are more densely sampled than others. These factors affect the detectability of all protoclusters, with those having smaller angular sizes or situated near the center of DESI pointings being most impacted. Consequently, our main objective in this study is not to confirm all protoclusters in these fields but to reliably identify protoclusters that are well characterized by the DESI data. Therefore, our analysis in this work is limited to structures which show significant overdensities in the 3D reconstruction. As a result, our search is biased towards the largest and most massive protoclusters in these regions.

In this work, we report five newly identified protoclusters based on DESI–ODIN spectroscopy. In addition, we confirm a sixth structure previously reported by G20 using existing spectroscopic redshifts and tomographic redshift estimates described in Section 3. In reconstructing its structure, we utilize both spectroscopic and tomographic redshifts to determine redshift priors for the probabilistic reconstruction.

The key properties of the six identified structures are summarized in Table 2, including their positional centers, the numbers of photometric and spectroscopic LAEs along each protocluster sightline, the estimated protocluster volumes, and the inferred descendant masses. Their sky locations are also shown in Fig-

Table 2. Summary of Six Protoclusters and their Substructures

Structure ID	R.A. ^a [degree]	Decl. ^a [degree]	z_{peak}^a	$N_{\text{spec, peak}}$	V_{PC}^b [10^3 cMpc^3]	$\log M_{\text{est}}^{z=0}/M_{\odot}^c$
COSMOS-z3.1-B <i>Center:</i> (149.80°, 1.47°) $N_{\text{spec}} = 174, N_{\text{LAE}} = 444$						
COSMOS-z3.1-B1	149.882 ± 0.161	1.378 ± 0.050	3.126 ± 0.012	32	19.8	15.2
COSMOS-z3.1-B2	149.475 ± 0.435	1.567 ± 0.036	3.110 ± 0.004	10	4.3	14.6
COSMOS-z2.4-A <i>Center:</i> (149.71°, 3.25°) $N_{\text{spec}} = 284, N_{\text{LAE}} = 402$						
COSMOS-z2.4-A1	149.852 ± 0.117	3.200 ± 0.100	2.452 ± 0.007	49	14.0	14.9
COSMOS-z2.4-A2	149.515 ± 0.042	3.306 ± 0.050	2.439 ± 0.003	8	4.3	14.4
COSMOS-z2.4-B <i>Center:</i> (150.00°, 1.27°) $N_{\text{spec}} = 183, N_{\text{LAE}} = 320$						
COSMOS-z2.4-B1	149.970 ± 0.057	1.439 ± 0.052	2.456 ± 0.005	12	7.7	14.6
COSMOS-z2.4-B2	150.035 ± 0.093	1.179 ± 0.055	2.437 ± 0.005	21	7.1	14.6
XMM-z2.4-A <i>Center:</i> (36.10°, -3.60°) $N_{\text{spec}} = 150, N_{\text{LAE}} = 377$						
XMM-z2.4-A1	36.029 ± 0.146	-3.625 ± 0.070	2.428 ± 0.005	27	16.9	15.2
XMM-z2.4-A2	36.340 ± 0.027	-3.728 ± 0.022	2.441 ± 0.002	3	0.8	13.8
XMM-z2.4-B <i>Center:</i> (36.15°, -4.40°) $N_{\text{spec}} = 158, N_{\text{LAE}} = 708$						
XMM-z2.4-B	36.162 ± 0.105	-4.533 ± 0.098	2.450 ± 0.011	17	16.5	15.0
XMM-z3.1-A <i>Center:</i> (34.80°, -5.20°) $N_{\text{spec}} = 73, N_{\text{tommo}} = 33, N_{\text{LAE}} = 433$						
XMM-z3.1-A1	35.006 ± 0.101	-5.159 ± 0.093	3.121 ± 0.006	7	17.9	15.2
XMM-z3.1-A2	34.574 ± 0.027	-5.216 ± 0.102	3.115 ± 0.006	19	15.0	15.1

^aThe centroid of each peak estimated from the 3D reconstruction. The uncertainties are computed as the density-weighted second moment of the positions of the voxels.

^bThe volume of the density peak above a density threshold of 97%, see text

^cThe uncertainty in the estimated descendant mass is ~ 0.2 – 0.3 dex.

ure 1. In all but one case, we identify two or more substructures that are spatially adjacent or interconnected; for these, we list the same parameters separately for each density peak. In some cases, depending on the proximity of the subgroups and the total mass contained within the system, the subgroups may merge into a single massive cluster by $z = 0$. Consequently, the summed masses of the subgroups should be regarded as a lower limit on the total descendant mass of the eventual merged system. For each protocluster field shown in Figures 3-8 (typically 1° on a side), we also report the total numbers of photometric LAEs (N_{LAE}) and DESI-confirmed galaxies (N_{spec}), as well as the subsets of each that lie within the defined protocluster volumes.

Smaller substructures likely exist, as was the case for COSMOS-z3.1-A and COSMOS-z3.1-C, which were studied in greater detail with targeted spectroscopy (Ramakrishnan et al. 2025b). However, the generally lower spectroscopic sampling density here makes it challenging to identify smaller and/or subtler features.

Four of the structures listed in Table 2 have a total mass $\log(M/M_{\odot}) \gtrsim 15$. Including COSMOS-z3.1-A,

COSMOS-z3.1-C, and the *Hyperion* proto-supercluster (Cucciati et al. 2018, indicated in green in Figure 1), a total of seven such structures have been identified within the ODIN-DESI area. The total cosmic volume spanned by these data is $\sim 1.6 \times 10^7 \text{ cMpc}^3$ (Ramakrishnan et al. 2025a). Assuming a Sheth & Tormen (1999) halo mass function, the number density of halos with $\log(M/M_{\odot}) \gtrsim 15$ at $z = 0$ is expected to be $\sim 2.2 \times 10^{-7} \text{ cMpc}^{-3}$; we would thus expect ≈ 4 such structures within the current ODIN volume, consistent with our present results.

In Ramakrishnan et al. (2025b), we defined a naming convention for spectroscopically confirmed ODIN protoclusters to be the field name, redshift, followed by a unique letter connected by a hyphen, and reported the discovery of COSMOS-z3.1-A and COSMOS-z3.1-C. Combined with this work, eight ODIN protoclusters have been spectroscopically confirmed.

5. ODIN STRUCTURES IN 3D

In this section, we discuss each of the six protoclusters in further detail, whenever possible, in the context

COSMOS-z3.1-B

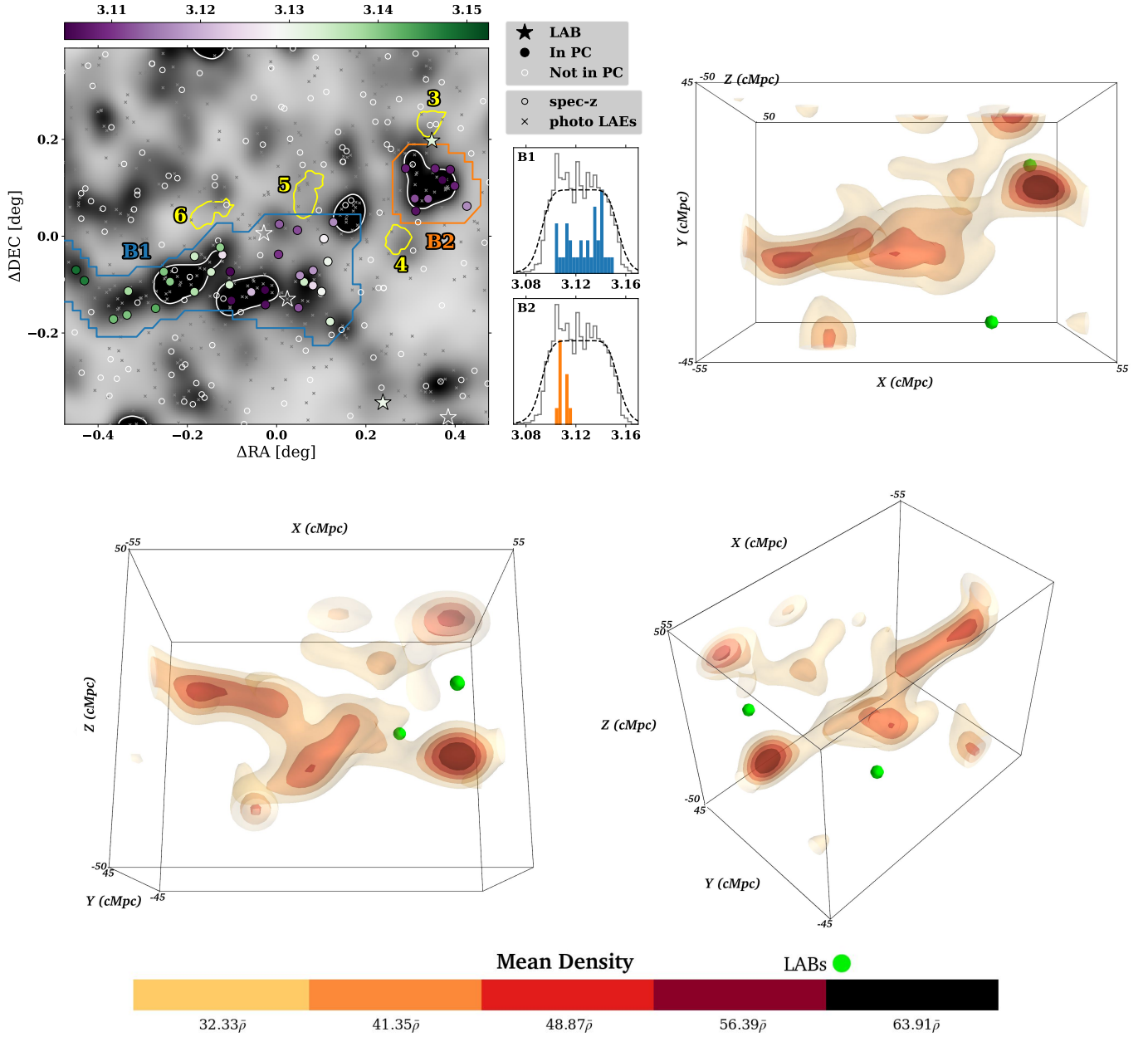


Figure 3. Top left: LAE surface density map around COSMOS-z3.1-B, shown in greyscale as in Figure 1; the pointing center is listed in Table 2. Blue and orange contours mark the projected 3D density peaks B1 and B2, while white contours indicate protocluster candidates identified from the 2D LAE overdensity map (Ramakrishnan et al. 2024, 2025a). LAEs with spectroscopic redshifts in B1 and B2 are shown as filled circles, color-coded by redshift; spectroscopic sources that fall outside these 3D density peaks are shown as open circles. LABs are shown as stars, and all photometric LAEs as grey crosses. Yellow contours denote protocluster candidates identified by (Toshikawa et al. 2024). Side panels show the redshift distributions of confirmed galaxies in each 3D peak (colored histograms), with the overall distribution shown in grey and the filter transmission curve as a dashed line. Top right: Reconstructed 3D model of COSMOS-z3.1-B viewed along the same line of sight, with densities relative to the mean field indicated by the color bar; confirmed LABs are shown as green spheres. Bottom panels show the 3D model from two additional viewing angles.

of other available data in their sightline. It is worth noting that one structure is identified as an LBG-rich protocluster candidate by another survey, another falls in a field with IGM tomography data, and the third harbors a massive ($M_{\text{star}} \approx 10^{11.2} M_{\odot}$) quiescent galaxy.

5.1. COSMOS-z3.1-B

This structure was first identified by Ramakrishnan et al. (2023) as one of the three most significant peaks, designated as *Complex B* in their study. COSMOS-z3.1-B is probably the second largest structure in this analysis (Table 2). In the 2D density map (shown as greyscale and white contours in the top left panel of Figure 3), the primary overdensity stretches from east to west and is distinct from two other overdensities to the northwest. The 3D reconstruction indicates that the main overdensity is composed of two broadly connected structures (labeled ‘B1’), where the eastern section is more distant from us compared to the western section and the northwestern peak (‘B2’). This is best illustrated in the bottom left panel, which shows the line-of-sight (Z) direction.

Three LABs are found near COSMOS-z3.1-B away from the highest density peaks, one of which has been confirmed by Moon et al. (2025) at $z \approx 3.133$ near density peak B2. Although appearing to lie within an overdense region in projection, the blob is ~ 20 cMpc behind the peak.

Recently, Toshikawa et al. (2024) identified protocluster candidates as overdensities of Lyman break galaxies (LBGs) in the deep and ultra-deep fields of the Subaru Strategic Program (Aihara et al. 2022). Given that the redshift selection of LBGs is much broader ($\Delta z \sim 0.6$) than that of LAEs ($\Delta z \sim 0.06$, corresponding to $\Delta d_{\text{LOS}} \sim 60$ cMpc), only the highest density “cores” regions are expected to be detected. In the top left panel of Figure 3, we reproduce the 2σ contours of four protoclusters identified by Toshikawa et al. (2024) as yellow contours, labeled with their ID numbers following their Table 2. These four are among the nine protoclusters they identified within the full ≈ 8 deg² extended COSMOS field at $z \sim 2.6 - 3.6$.

Intriguingly, these four protocluster candidates are found within this relatively small ($\approx 1^{\circ} \times 0.8^{\circ}$) section of the field, mere arcminutes away from COSMOS-z3.1-B. Moreover, the LBG- and LAE density peaks appear to systematically avoid one another, although, if any of the former lie at the same redshift as the latter, it is expected that the true extent would be likely much larger and therefore would overlap significantly with COSMOS-z.3.1-B.

We consider possible scenarios. First, the observed angular proximity could be attributed to the projection effect, indicating that the four LBG protoclusters are not in close physical proximity to COSMOS-z.3.1-B. A high concentration of LBG-rich protoclusters may be due to cosmic variance since protoclusters show strong clustering (Toshikawa et al. 2018; Ramakrishnan et al. 2025a). One of these protoclusters, *ID5*, has been confirmed to be a protocluster at $z \approx 3.05$ (J. Toshikawa, private communication), placing it in the foreground relative to density peak B1. Given that the line-of-sight separation between COSMOS-z3.1-B1 and *ID5* is more than 70 cMpc, they are unlikely to be associated with each other.

Alternatively, one or more of the LBG-rich protoclusters could be genuinely associated with COSMOS-z.3.1-B. How LBGs and LAEs trace the LSS is still poorly understood. Shi et al. (2019) reported a segregation of an LAE and LBG overdensity and speculated that the latter may be dominated by more evolved and more massive galaxy constituents perhaps due to an early formation time. Using cosmological simulations, Im et al. (2024) demonstrated that LAEs and LBGs can occupy the same LSS while appearing spatially distinct due to selection effects and galaxy bias. In contrast, in a few best-known protocluster systems such as SSA22 and *Hyperion*, LAEs and LBGs appear to coexist (e.g., Cucciati et al. 2018; Huang et al. 2022). Targeted spectroscopy of galaxies belonging to these regions of overdensities will be needed to obtain a clear picture.

5.2. COSMOS-z2.4-A

Like COSMOS-z3.1-A and B, this structure is extended in the transverse (sky) direction, stretching $\approx 90 \times 80$ cMpc² at $z \approx 2.45$. However, it is a substantially less massive and smaller protocluster than COSMOS-z3.1-A⁵ and COSMOS-z3.1-B. As illustrated in Figure 4, we have identified two main density peaks that are closely grouped in redshift space. The southern portion of the larger, more massive group ‘A1’ ($\log M_{\text{est}}^{z=0}/M_{\odot} \approx 14.9 \pm 0.2$) curves slightly in our direction, while the smaller, less massive group ‘A2’ lies closer to us and sits 15 cMpc from it in 3D space.

COSMOS-z2.4-A is notably blob-rich, showing five LABs along its sightline and several more at a distance. Of these, four have been confirmed by DESI. Similar to the trend observed in Ramakrishnan et al. (2025b), the confirmed blobs, while proximate to the 3D density

⁵ As described in Ramakrishnan et al. (2025b), COSMOS-z3.1-A spans $\sim 140 \times 140$ cMpc² in the sky direction with the descendant mass a few times larger than the present-day Coma cluster.

COSMOS-z2.4-A

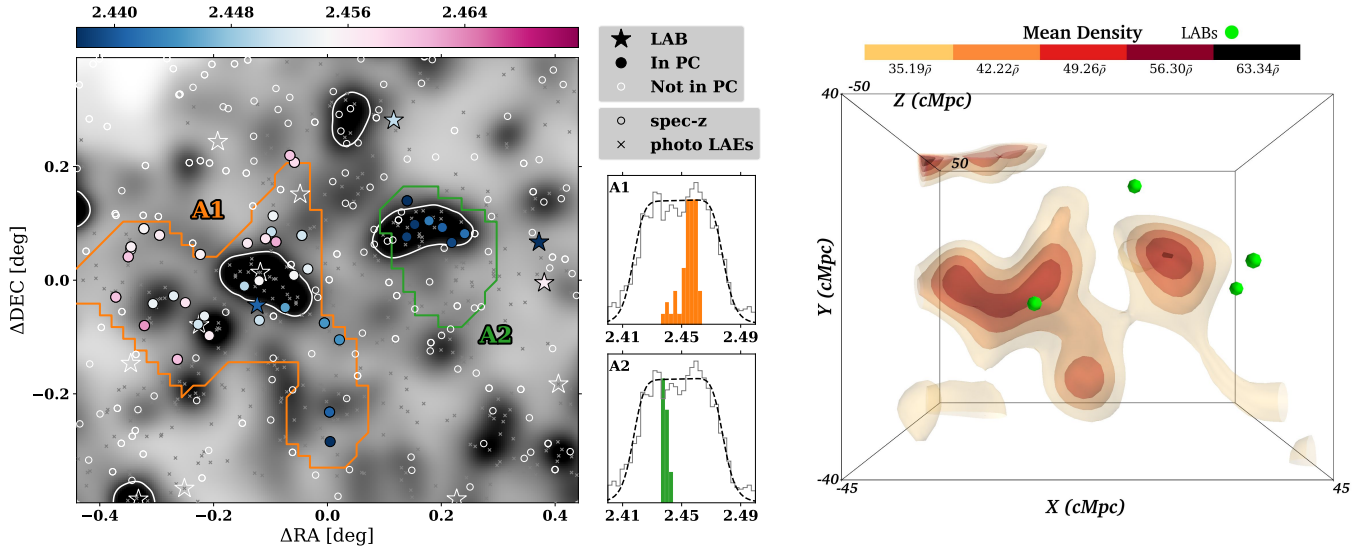


Figure 4. Similar to Figure 3, but for COSMOS-z2.4-A.

peaks, seem to avoid their cores and instead reside at the outskirts.

The 3D reconstruction shows a filamentary extension originating from peak A2 towards the bottom-right corner of the volume. This feature is not apparent in the 2D surface density map, as filaments correspond to extended, moderate overdensities that are diluted by line-of-sight projection (Ramakrishnan et al. 2024). However, several spectroscopically confirmed LAEs outside the protocluster density peaks (open circles) trace the projected path of this feature. This filament is also detected when we run the filament finder software, DisPerSE (Sousbie 2011), in both the 2D distribution of photometric LAEs and 3D (utilizing sky positions and redshift of the confirmed LAEs). Ramakrishnan et al. (2024) used the IllustrisTNG simulation suite to show that the detection of cosmic filaments via DisPerSE is highly robust.

5.3. COSMOS-z2.4-B

Figure 5 illustrates the structure as consisting of two groups with similar masses, estimated at $\log M_{\text{est}}^{z=0}/M_{\odot} \approx 14.6 \pm 0.2$ each (Table 2). Group B1 is located to the north and is more distant from us than Group B2. In both the 2D and 3D density maps, B2 appears to contain two smaller subcomponents that, at the adopted 3D density threshold, merge into a single connected system. Our LAB selection identifies three blobs in this region (Moon et al. 2025), but only one is spectroscopically confirmed at $z \approx 2.445$. The connection between it and COSMOS-z2.4-B remains undetermined because of the absence of spectroscopy in the region.

5.4. XMM-z2.4-A

Although XMM-z2.4-A lies near the northern boundary of the ODIN footprint, DESI spectroscopic coverage extends beyond this region. The full spatial extent of the structure beyond the surveyed area remains unconstrained. Figure 6 illustrates five distinct 2D overdensities (marked by white contours). The 3D reconstruction identifies four of these as interconnected systems at $z \approx 2.425$, while the fifth lacks spectroscopic data. Despite our detection picking up two distinct systems, group A2 is likely at the tip of A1 as it curves away from our viewpoint. With $\log M_{\text{est}}^{z=0}/M_{\odot} \gtrsim 15.2$, XMM-z2.4-A stands as one of the most massive systems found in this study. Within this subfield, two LABs have been confirmed: one is situated farther back at $z \approx 2.46$, and the other resides near the core of A1. The latter is unusual because, as Ramakrishnan et al. (2023) reported, LABs tend to be found at the outskirts of protoclusters.

5.5. XMM-z2.4-B

Located in the ultradeep portion of the field, XMM-z2.4-B lies within the footprint of the Ly α Tomography IMACS Survey (LATIS; Newman et al. 2020). LATIS uses background QSOs and galaxies to map the H I opacity of the intergalactic medium at $z = 2.2\text{--}2.8$, based on the Ly α forest region of the spectra (i.e., $\lambda_{\text{rest}} \sim 1026\text{--}1200 \text{ \AA}$), achieving a spatial resolution of 3–4 cMpc. Within a $\approx 0.6 \text{ deg}^2$ subregion of the XMM-LSS field, Newman et al. (2025a) identified seven protoclusters. Three of these fall within the redshift range probed by the N419 filter – LATIS2_D1.00, LATIS2_D1.01, and LATIS2_D1.05—at $z = 2.452, 2.455,$ and 2.440 , respectively (see their Ta-

COSMOS-z2.4-B

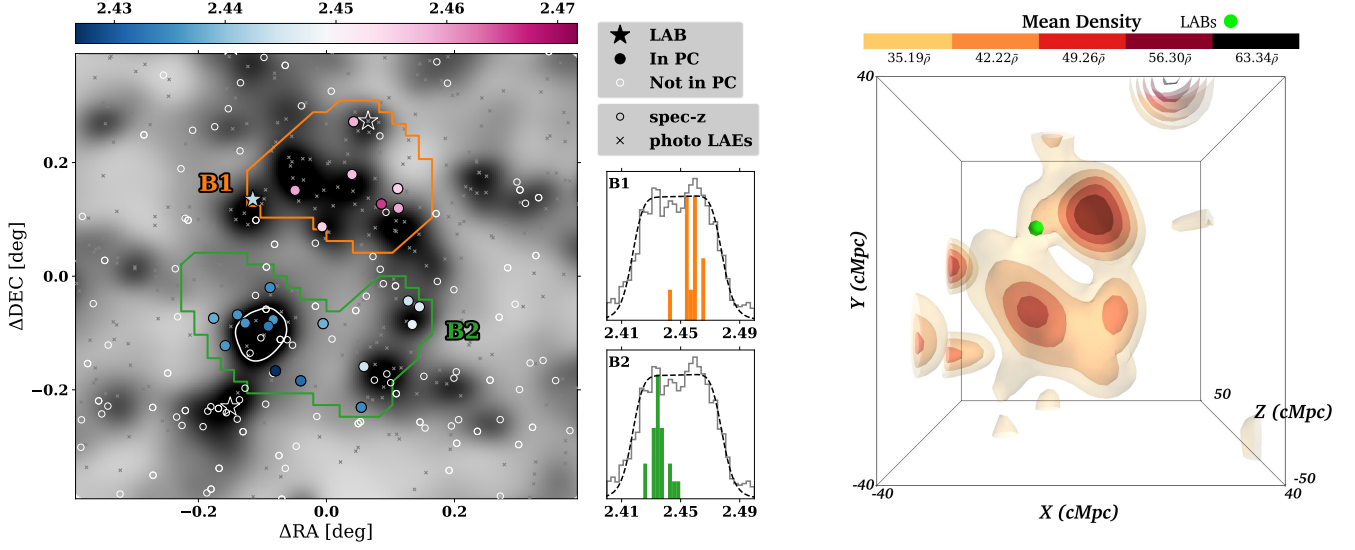


Figure 5. Similar to Figure 3, but for COSMOS-z2.4-B.

XMM-z2.4-A

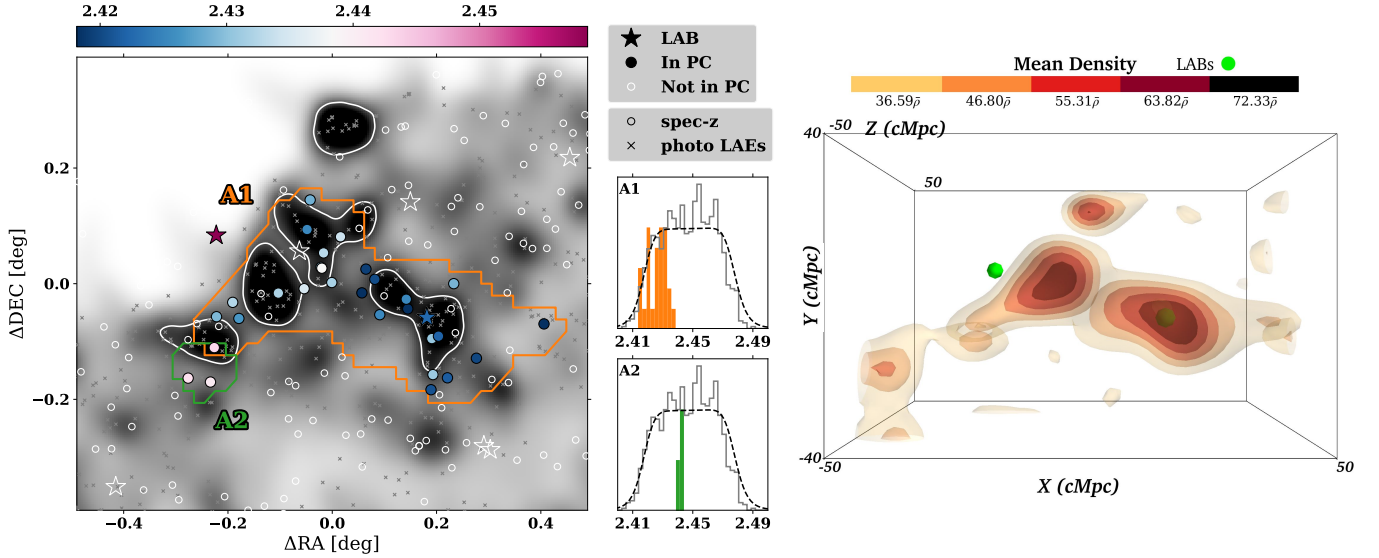


Figure 6. Similar to Figure 3 but for XMM-z2.4-A.

ble 1). Among the 37 density peaks identified across the full 1.7 deg^2 LATIS survey area, these rank 3rd, 7th, and 30th, respectively, in terms of the measured Ly α transmission deficit,⁶ indicating that they correspond to regions of relatively high H I density in that order.

⁶ Specifically, the ranking is based on $\delta_F/\sigma_{\text{map}}$, where δ_F is the Ly α transmission fluctuation at a given 3D location, defined as $\delta_F \equiv F/\langle F \rangle - 1$. Here F is the measured transmitted Ly α flux, $\langle F \rangle$ is the mean transmission, and σ_{map} is the standard deviation of δ_F across the field.

In Figure 7, we present the projected 3D contours of XMM-z2.4-B (orange solid line) alongside the $\delta_F/\sigma_{\text{map}}$ contours from LATIS (green dashed lines), LBG surface-density contours (yellow dotted lines), and the positions of individual LBGs and QSOs from LATIS (diamonds). Two redshift slices are shown: $z = 2.455 \pm 0.001$ (top left) and $z = 2.451 \pm 0.001$ (bottom left). The centers of H I overdensities are indicated by large green crosses, labeled with their abbreviated LATIS IDs. Among these, LATIS2_D1.01 exhibits substantial—though not perfect—overlap with XMM-z2.4-B in both redshift and projected extent. Notably, its peak position (green

XMM-z2.4-B

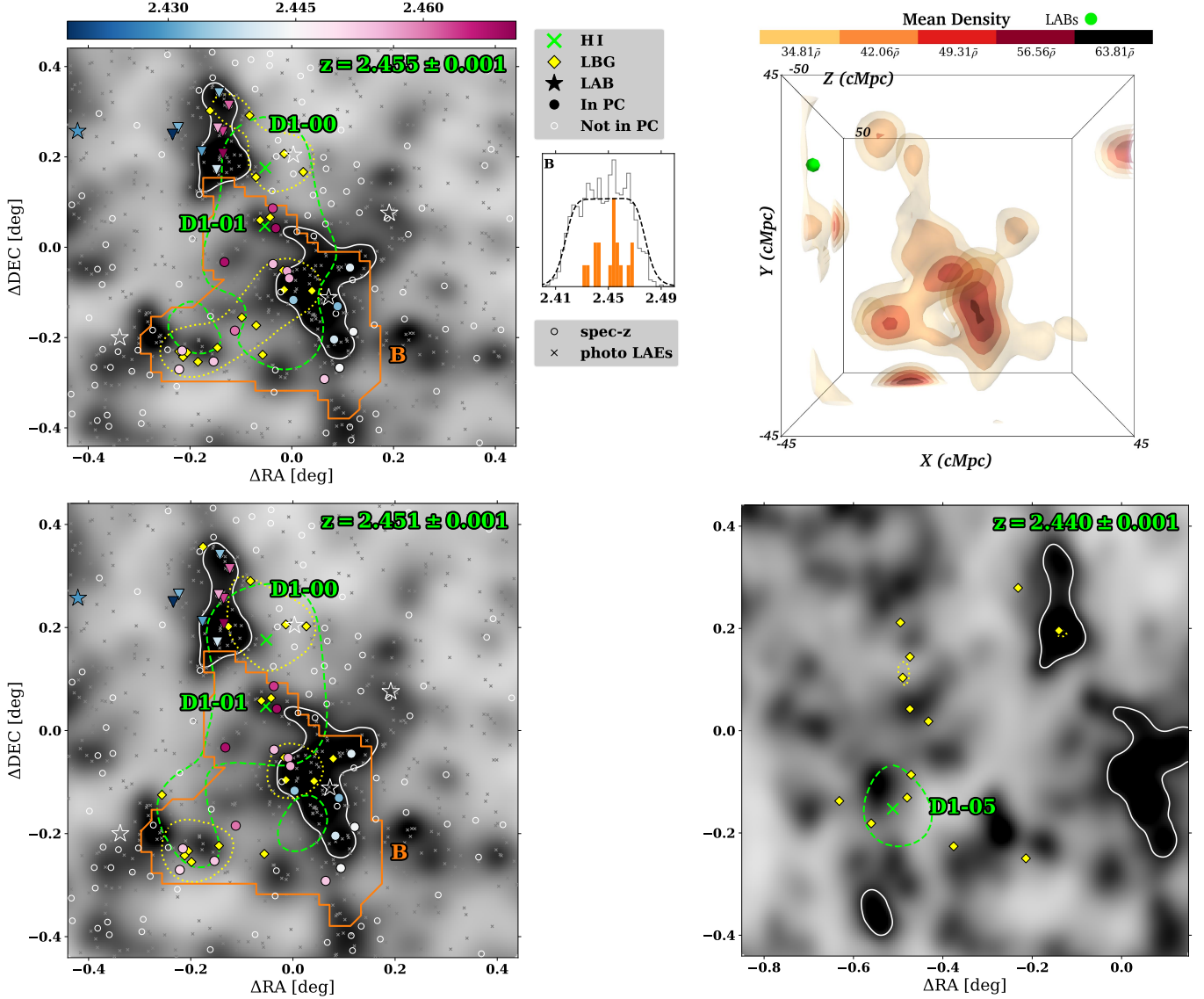


Figure 7. Similar to Figure 3 but for XMM-z2.4-B. In the top left, bottom left, and bottom right panel, green dashed contours mark the projected 3D contours of the highest $\delta_F/\sigma_{\text{map}}$ peaks reported by LATIS in three redshift slices corresponding to D1-00, D1-01, and D1-05, respectively, whose centers are indicated by green crosses. In the bottom right panel, the field center is shifted by ≈ 0.5 deg eastward to show D1-05. The background greyscale is the 2D LAE surface density map and crosses denote LATIS and H I peaks, respectively. Yellow dotted contours and diamonds indicate LBG surface density and individual LBG/QSO positions at these redshift slices from LATIS. The downward triangles in the two left panels mark spectroscopic sources overlapping with D1-00; while these sources are not formally part of XMM-z2.4-B in our 3D detection, they reside in a 2D-selected protocluster whose angular extent overlaps significantly with D1-00 (see text for more discussion).

cross) is slightly offset eastward from the region of highest LAE density, shown by the white contour. A similar spatial relationship between LAEs, LBGs, and H I overdensities has been noted in previous Ly α forest tomography work (Momose et al. 2021; Newman et al. 2025a), where LAEs tend to be offset from the highest H I peaks traced by LBGs.

The sky position of LATIS2_D1.00 lies near another LAE overdensity to the north, which is not formally identified as a protocluster by our selection method and is not part of XMM-z2.4-B. Spectroscopically confirmed galaxies in this northern region are shown as downward-pointing triangles in the left panels of Figure 7. None of the LAEs in the highest-density area near the center of LATIS2_D1.00 have spectroscopic confirmation,

while those with measured redshifts are roughly evenly divided between $z \approx 2.425$ and $z \approx 2.455$ – 2.460 . This redshift split, combined with the limited number of confirmed sources, likely led us to miss any structures that may exist in this area. Although additional spectroscopy around LATIS2_D1_00 is required, it is plausible that it is associated with a yet-to-be-confirmed LAE-rich structure.

In the bottom right panel of Figure 7, we show the LAE density map around the third H I-selected overdensity, LATIS2_D1_05, located $\sim 0.5^\circ$ east of XMM-z2.4-B. We do not detect any significant 3D structure in this region, although it may coincide with a relatively modest LAE overdensity. This is consistent with the relatively low ranking of LATIS2_D1_05 (30th out of 37 H I-selected overdensities), suggesting that it traces a much smaller and less prominent structure compared to the other two.

5.6. XMM-z3.1-A

The location of XMM-z3.1-A lies in a part of the field that is not covered by DESI-ODIN spectroscopy since DESI has allocated it for different targets. We combine follow-up spectroscopy from G20 alongside tomographic redshift estimates, as detailed in Section 3, to perform 3D detection and analysis of XMM-z3.1-A. Since the majority of objects have tomographic redshifts rather than spectroscopic ones, the effective line-of-sight resolution in our reconstruction is set by the tomography scatter (see Section 3). In Figure 8, these redshifts are represented by various symbols.

We identify two structures with descendant masses of similar magnitude ($\log M_{\text{est}}^{z=0}/M_\odot \approx 15.1 - 15.2$). Together, they include four separate LAE surface overdensities shown as white contours. The boundaries of these structures are merely 2–3' apart. Structure A1 seems to have a dense core, with its tail extending towards the northeast, although further spectroscopy is required for confirmation. Meanwhile, the densest part of A2 is situated at its northern extremity, with the tail extending linearly southward, curving slightly in our direction. Three LABs have been identified, all near the northern area, though none have been spectroscopically confirmed.

Located at the northern end of A2 is a massive, quiescent galaxy (MQG) known as 3D-UDS-41232, which is among the 19 massive galaxies confirmed by Nanayakkara et al. (2025). UDS-41232 ranks second in their list in stellar mass with $M_{\text{star}} \approx 1.2 \times 10^{11} M_\odot$, and its spectral energy distribution is consistent with a passive galaxy, with the time-averaged star formation rate over the past 100 million years being much less

than $0.1 M_\odot \text{ yr}^{-1}$. Intriguingly, 3D-UDS-41232 is situated just outside the region of the highest LAE surface density. One LAB lies close to this MQG in projection, though the lack of its redshift prevents us from assessing any potential physical association between the two. While further spectroscopy is necessary for a detailed study, it is significant to note that this represents one of the first known occurrences of an ultramassive quiescent galaxy within its large-scale structural context.

6. LY α LINE FLUX AS A FUNCTION OF ENVIRONMENT

In dense protocluster environments, Ly α line fluxes may vary for different reasons. First, a steadier and robust supply of pristine gas may lead to a higher star formation rate, star formation efficiency, and/or younger stellar ages, thereby increasing Ly α photon production relative to the average environment. However, a higher star formation activity is expected to be accompanied by increased production of dust, which might offset or even reverse the trend. Second, regions of large-scale galaxy overdensities are expected to be also overdense with H I gas as they correlate with each other (e.g., Liang et al. 2021; Momose et al. 2021; Newman et al. 2025b) although opposite examples also exist (Liang et al. 2025). In this context, the radiative transport process in protoclusters may be such that Ly α photons in their cores have shorter mean free paths and a higher likelihood of being absorbed or scattered (e.g., Shimakawa et al. 2017; Momose et al. 2021).

Indeed, previous studies reported different Ly α properties in protocluster galaxies but their conclusions did not always agree (e.g., Shi et al. 2019; Lemaux et al. 2022). Based on two confirmed protoclusters, Dey et al. (2016) reported that Ly α fluxes in protocluster galaxies are on average $\approx 35\%$ higher than non-protocluster counterparts, hinting that the effect may be non-negligible. Since both target selection and spectroscopic confirmation are based on the line brightness, this ‘luminosity bias’ will impact both at the protocluster scales. More recently, Nagaraj et al. (2025) measured Ly α luminosity functions at $z \sim 2.4, 3.1, \text{ and } 4.5$ based on ODIN LAE samples, finding that galaxies identified in 2D-selected protoclusters (Ramakrishnan et al. 2024) have shallower faint-end slopes α relative to the average field galaxies.

Related trends have also been identified in simulations. Using TNG100 and TNG300, Andrews et al. (2025) found an excess of bright UV-selected galaxies in protocluster regions and a noticeably flatter faint-end slope in the UV luminosity function compared to the field, while the corresponding effect in the Ly α luminosity function was present but significantly weaker.

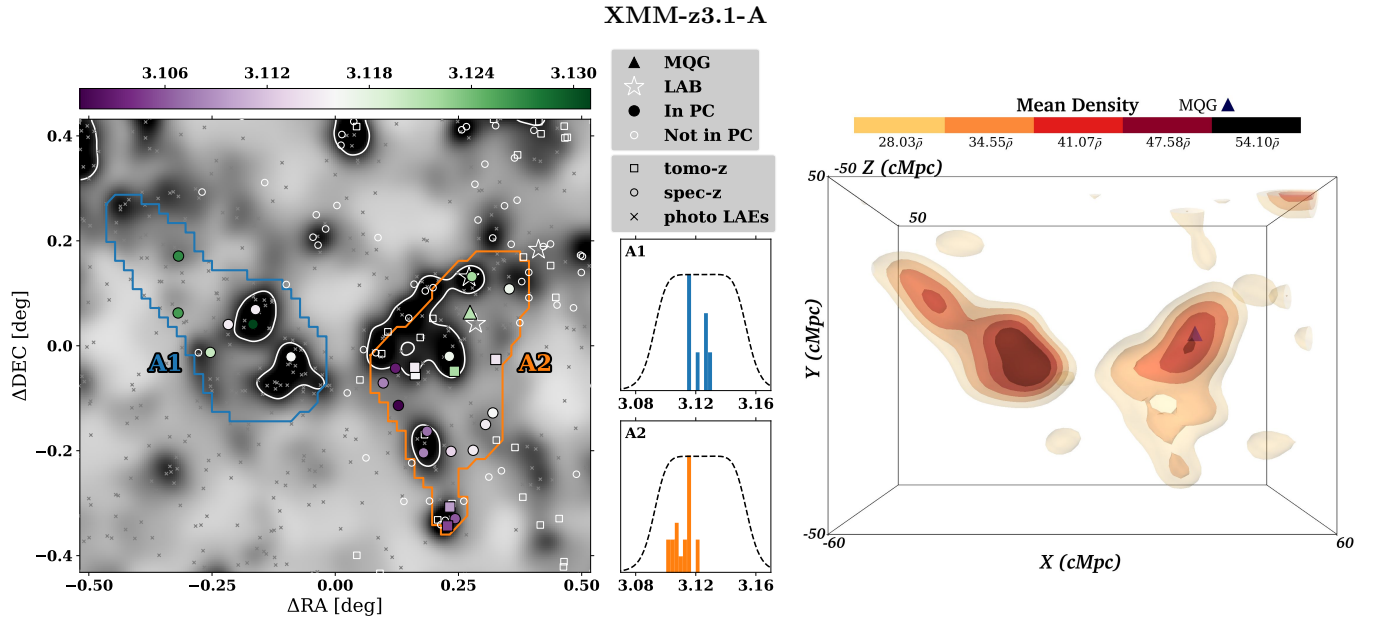


Figure 8. As Figure 3, for XMM-z3.1-A. 3D-UDS-41232, a massive quiescent galaxy at $z = 3.121$ (Nanayakkara et al. 2025) is shown as a triangle. *Left:* LAEs with redshifts spectroscopically confirmed are shown as circles, while redshifts estimated through tomography are shown in squares.

Leveraging the robust sample of protocluster member galaxies identified in this study, we analyze the differences in line flux between LAEs found in average environments and those in protocluster environments. We measure $\text{Ly}\alpha$ line fluxes by fitting each spectrum within $\pm 40 \text{ \AA}$ of the central wavelength of the narrowband filter, assuming a two-component model with a linear continuum and a skew-normal function⁷ to capture the $\text{Ly}\alpha$ emission line. Once the best-fit is obtained, the line flux is estimated by simply integrating the skew-normal function. Given the limited depth of the spectroscopic observations, for the majority of the LAEs, the continuum fluxes are consistent with zero within the uncertainties. The best-fit continuum model does not change the line flux.

We examine how the large-scale environment affects the $\text{Ly}\alpha$ line fluxes of galaxies. Since protoclusters have been defined in both two dimensions (Ramakrishnan et al. 2025a) and three dimensions (Section 4; see also Ramakrishnan et al. 2025b), we assess environmental trends using both definitions. For clarity, we summarize the criteria here. 2D protoclusters are identified as contiguous regions with projected overdensity $\delta_{\text{LAE},2\text{D}} > 2.3$ (2.6) at $z \approx 2.4$ (3.1) with the projected angular size $> 40 \text{ cMpc}^2$. 3D protoclusters are defined as contiguous volumes in the reconstructed den-

sity field that exceed the 97th percentile overdensity and enclose $> 500 \text{ cMpc}^3$. Figure 9 shows the spectroscopically confirmed LAEs used in this analysis, plotted in the $\delta_{\text{LAE},2\text{D}} - \delta_{\text{LAE},3\text{D}}$ parameter space. Galaxies identified as members of 2D (3D) protoclusters are marked by open (filled) circles. Field galaxies, shown as grey circles, are defined to have $\delta_{\text{LAE},2\text{D}} \leq 1.0$ (1.3) at $z \approx 2.4$ (3.1), which encloses the bottom half in 2D density. By doing so, we ensure that no galaxy near a 2D or 3D protocluster is included in the field sample. The rest, belonging to neither our 2D/3D protocluster sample nor the field sample, indicated by smaller grey dots in Figure 9, are not used in the subsequent analysis.

The relatively large scatter between $\delta_{\text{LAE},2\text{D}}$ and $\delta_{\text{LAE},3\text{D}}$ is readily understood. Our 3D detection algorithm is tuned to identify the entire volume of an overdensity that is likely to collapse into a single halo by $z = 0$, ensuring that the corresponding descendant mass estimate approximates $M_{200}^{z=0}$. As demonstrated in Ramakrishnan et al. (2024), this approach recovers the present-day halo mass to within 0.15 dex. Consequently, a galaxy can occupy a region of high 3D density while still lying outside the local 2D density peak projected on the sky.

This behavior is illustrated in Figures 3–8, where the reconstructed 3D protocluster boundaries are shown as colored contours and the 2D photometric protoclusters are outlined in white. In contrast, the galaxies within 2D-selected protoclusters should trace the highest surface densities but contain some interlopers – located in

⁷ A skew-normal function is defined as a normal distribution with an additional skew parameter α which controls the symmetry of the curve.

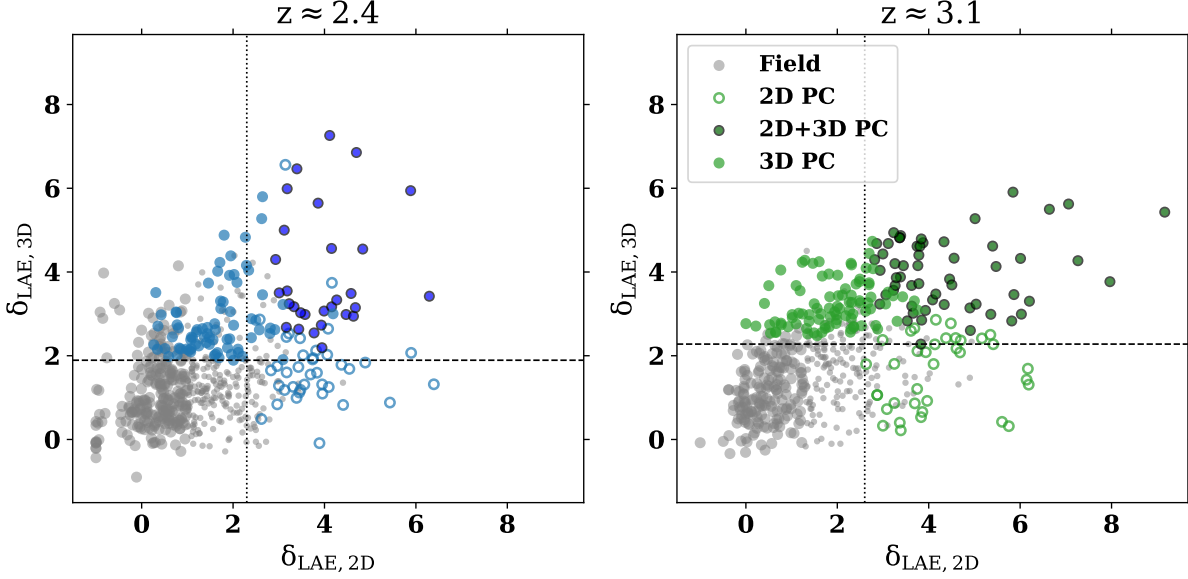


Figure 9. Comparison of overdensities in 2D and 3D space for LAEs at $z \approx 2.4$ (left) and $z \approx 3.1$ (right). Each point indicates an individual LAE, color-coded by its protocluster classification. Open (filled) circles denote member of the 2D (3D) sample only, and filled circles with a black outline denote members of both 2D and 3D protoclusters. Grey circles are field galaxies, while smaller grey dots are galaxies not in any sample. The dashed line marks the corresponding $\delta_{\text{LAE}, 3\text{D}}$ threshold used to define 3D protoclusters, and the dotted line marks the $\delta_{\text{LAE}, 2\text{D}}$ threshold.

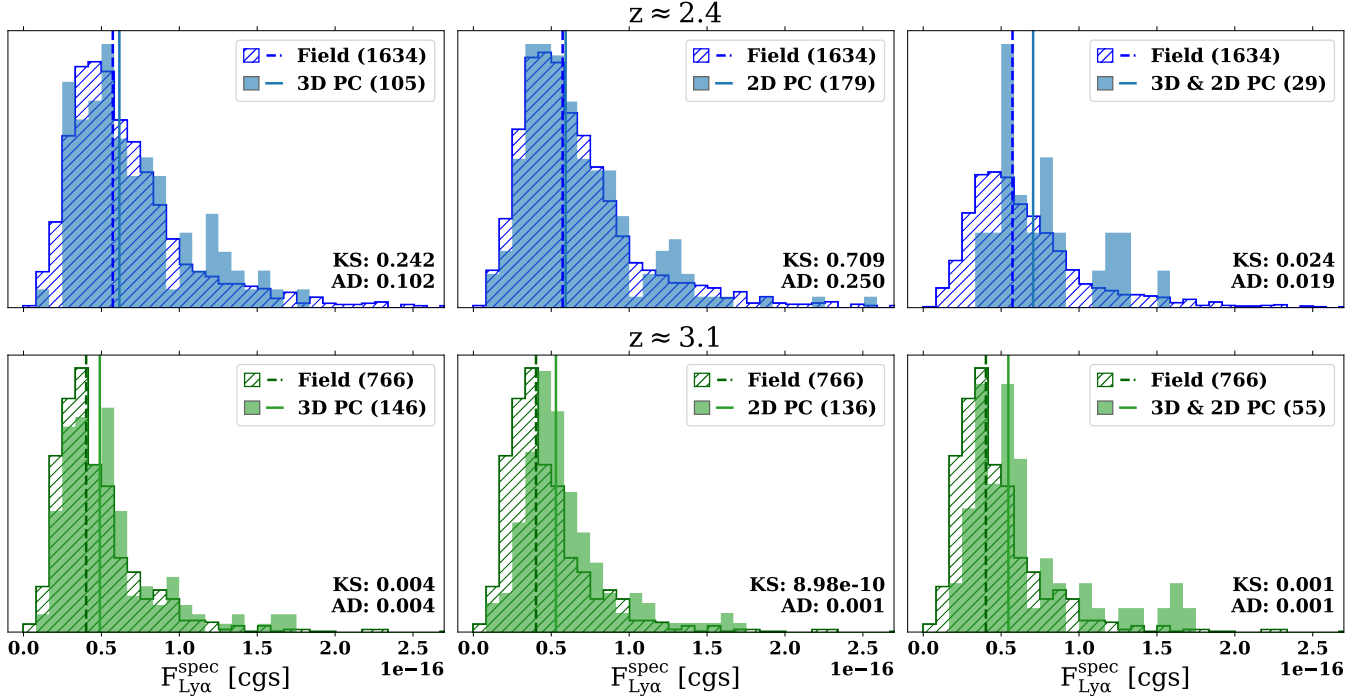


Figure 10. Histograms of $F_{\text{Ly}\alpha}^{\text{spec}}$ for protocluster (filled) and field (hatched) samples at $z \approx 2.4$ (top) and $z \approx 3.1$ (bottom). The left (middle) panels show 3D (2D) protocluster member galaxies, while the right panels show galaxies identified as members by both 2D and 3D selection. Field galaxies are chosen to have local density $\delta_{\text{LAE}, 2\text{D}}$ at the 50%-tile or below. Vertical solid (dashed) lines mark the median line fluxes of the protocluster (field) sample. The Kolmogorov-Smirnov (KS) and Anderson-Darling (AD) test p -values, comparing the two distributions, are listed in the bottom right of each panel.

the foreground or background relative to the true 3D structure – which dilute intrinsic correlations. In this sense, galaxies classified as members of *both* 2D and 3D protoclusters most likely reside in the densest cores of forming clusters.

In Figure 10, we compare the Ly α line-flux distributions of galaxies residing in protoclusters identified by the 3D (left), 2D (middle), and combined 2D+3D (right) methods with those of field galaxies. Each histogram is normalized to unit area for direct comparison. To test whether the protocluster and field samples are drawn from the same parent population, we apply both the Kolmogorov–Smirnov and Anderson–Darling tests; the resulting p -values are shown in the bottom right corner of each panel.

At $z \approx 3.1$, protocluster LAEs exhibit systematically higher Ly α fluxes than field galaxies, with the difference being statistically significant. Visual inspection and formal tests both indicate that this enhancement is most pronounced in the 2D and 2D+3D selections, while it appears weaker for the 3D case alone. This likely reflects the inclusion of galaxies near the edges of 3D protoclusters, where the local density is lower (see Figure 9). This suggests that not every protocluster member has a higher Ly α flux than most field galaxies. Although both the 2D and 2D+3D protocluster samples differ significantly from the field, the shift in median flux (vertical lines in Figure 10) is larger for the 2D+3D subset, consistent with the expectation that projection effects in purely 2D selections dilute the trend.

At $z \approx 2.4$, the difference between protocluster and field LAEs is less pronounced. The 3D-selected protoclusters show only a marginal trend, and the 2D sample shows little to no distinction from the field. This likely reflects increased contamination by environmental interlopers: projection effects in the 2D selection and the inclusion of galaxies in lower-density protocluster outskirts in the 3D selection both act to dilute intrinsic differences relative to the field. However, galaxies identified as 2D+3D members – those located in the densest protocluster cores – still show a statistically significant difference ($p \approx 0.02$), with an enhancement in median line flux comparable to that observed at $z \approx 3.1$.

Although the sample size is limited, our results suggest that galaxies in dense protocluster cores have Ly α flux distributions that are systematically skewed toward brighter values and show a relative deficit of faint emitters. This finding aligns with the shallower faint-end slope (α) of the Ly α luminosity function reported for (2D) protocluster regions by Nagaraj et al. (2025), although they acknowledged that the trend is marginal and larger sample sizes are needed to validate the trend.

Additionally, our results are fully consistent with those independently reported by Uzsoy et al. (2025), who also used the 2D-based protocluster selection (also see Huang et al. 2021). Additional spectroscopy will be needed to confirm this trend.

7. SUMMARY

Building on Ramakrishnan et al. (2025b), we extend the 3D reconstruction methodology in this work to identify and characterize massive protoclusters in the COSMOS and XMM-LSS fields. Our analysis combines a large sample of spectroscopically confirmed LAEs from DESI with an even larger catalog of photometric LAEs (Table 1). Our main findings are summarized as follows.

1. We confirm six massive protoclusters, five of which are newly identified using DESI–ODIN spectroscopy. The sixth structure is verified using a combination of spectroscopy from G20 and tomographic redshifts derived from two overlapping filters, NB497 and N501 (Section 3 and Figure 2). The reconstructed maps also reveal multiple substructures interconnected by lower-density filaments, suggestive of early-stage assembly within the cosmic web.
2. Three of the identified systems overlap with structures detected through other tracers, offering insight into how different galaxy populations and intergalactic gas trace the underlying large-scale structure (Section 5).
 - *COSMOS-z3.1-B*: Located within a region rich in LBGs (Toshikawa et al. 2024, Figure 3), the LAE and LBG surface density maps show a modest offset, which may be attributed to different selection effects of LAE- and LBG-based protocluster detections, or alternatively, the projection effect of physically unrelated cosmic structures. The only LBG structure with spectroscopic confirmation lies ≈ 70 cMpc in the foreground, and thus is unlikely to be associated with COSMOS-z3.1-B. Follow-up spectroscopy is needed to clarify the physical connection of the remaining structures.
 - *XMM-z2.4-B*: This structure overlaps with H I tomographic mapping and LBG overdensities from LATIS, showing significant spatial alignment among LAE-, LBG-, and H I-selected high-density regions (Figure 7).
 - *XMM-z3.1-A*: It is possibly the most massive structure identified in this study as its estimated descendant mass rivals that of the Coma cluster. A spectroscopically confirmed massive ($M_{\text{star}} \approx$

$10^{11.2} M_{\odot}$) quiescent galaxy is located in the central region of a structure (A2: Figure 8). This discovery possibly marks one of the earliest known examples of environmental quenching at $z \sim 3$.

3. Using both 2D- and 3D-defined protocluster membership (Section 4.3), we compare Ly α fluxes in protocluster and field galaxies. By combining 2D and 3D density information, we isolate galaxies residing in the densest protocluster cores. At $z \approx 3.1$, these galaxies exhibit higher median Ly α line fluxes and a deficit of faint emitters compared to the field. Consistent with Uzsoy et al. (2025), no significant difference is found for $z \approx 2.4$ galaxies when selected purely by 2D overdensity. However, the 2D+3D-selected subset shows a comparable flux enhancement to that observed at $z \approx 3.1$, albeit with a smaller sample size. Overall, the contrast between protocluster and field populations is much stronger at $z \approx 3.1$ than at $z \approx 2.4$, suggesting possible redshift evolution in the environmental dependence of Ly α emission.
4. Of the six structures considered in this work, four are the progenitors of the most massive structures whose estimated descendant masses rival that of Coma at $\log(M^{z=0}/M_{\odot}) \gtrsim 15$ (Table 2). Together with the two protoclusters reported by Ramakrishnan et al. (2025b) and *Hyperion*, ODIN has identified a total of seven Coma progenitors within a volume of $\sim 1.7 \times 10^7$ cMpc³. The inferred number density is consistent with the theoretical expectation, demonstrating that ODIN is highly successful at identifying the high-redshift progenitors of the most massive structures.

Combined with Ramakrishnan et al. (2025b), this work brings the total number of spectroscopically confirmed ODIN protoclusters to eight, providing one of the first wide-field, 3D-mapped samples of massive protoclusters across Cosmic Noon.

DATA AVAILABILITY

All data shown in figures are available on Zenodo (doi: <https://doi.org/10.5281/zenodo.18436376>). Interactive 3D visualizations are available on GitHub (<https://ortiz140.github.io/odin/>).

ACKNOWLEDGMENTS

We thank Jun Toshikawa for helpful discussions. The authors acknowledge financial support from the U.S. National Science Foundation (NSF) under grant Nos. AST-

2206705, AST-2408359, and from the Ross-Lynn Purdue Research Foundations. This work is based on observations at Cerro Tololo Inter-American Observatory, NSF’s NOIRLab (Prop. ID 2020B-0201; PI: K.-S. Lee), which is managed by the Association of Universities for Research in Astronomy under a cooperative agreement with the National Science Foundation. M.C.A. and A.K. acknowledge financial support from ANID BASAL project FB210003 and ALMA fund with code 31220021. C.G. acknowledges support from the National Science Foundation under grant AST-2408358. L.G. gratefully acknowledges support from the FONDECYT regular project number 1230591, the ANID BASAL project FB210003, ANID - MILENIO - NCN2024.112. H.S.H. acknowledges the support of the National Research Foundation of Korea (NRF) grant funded by the Korea government (MSIT), NRF-2021R1A2C1094577, and Hyunsong Educational & Cultural Foundation. S.L. acknowledges support from the National Research Foundation of Korea (NRF) grant RS-2025-00573214, funded by the Korean government (MSIT). Y.Y. and B.M. are supported by the Basic Science Research Program through the National Research Foundation of Korea funded by the Ministry of Science, ICT & Future Planning (2019R1A2C4069803). H. Song was supported by the National Research Foundation of Korea (NRF) grant funded by the Korea government (MSIT) (No. RS-2025-25442707).

This material is based upon work supported by the U.S. Department of Energy (DOE), Office of Science, Office of High-Energy Physics, under Contract No. DE-AC02-05CH11231, and by the National Energy Research Scientific Computing Center, a DOE Office of Science User Facility under the same contract. Additional support for DESI was provided by the NSF, Division of Astronomical Sciences under Contract No. AST-0950945 to the NSF’s National Optical-Infrared Astronomy Research Laboratory; the Science and Technology Facilities Council of the United Kingdom; the Gordon and Betty Moore Foundation; the Heising-Simons Foundation; the French Alternative Energies and Atomic Energy Commission (CEA); the National Council of Humanities, Science and Technology of Mexico (CONACYT); the Ministry of Science, Innovation and Universities of Spain (MICIU/AEI/10.13039/501100011033), and by the DESI Member Institutions: <https://www.desi.lbl.gov/collaborating-institutions>. Any opinions, findings, and conclusions or recommendations expressed in this material are those of the author(s) and do not necessarily reflect the views of the U. S. National Science Foundation, the U. S. Department of Energy, or any of the listed funding agencies. The authors are hon-

ored to be permitted to conduct scientific research on

I'oligam Du'ag (Kitt Peak), a mountain with particular significance to the Tohono O'odham Nation.

REFERENCES

- Abdul Karim, M., Aguilar, J., Ahlen, S., et al. 2025, *PhRvD*, 112, 083515, doi: [10.1103/tr6y-kpc6](https://doi.org/10.1103/tr6y-kpc6)
- Adame, A. G., Aguilar, J., Ahlen, S., et al. 2025, *JCAP*, 2025, 028, doi: [10.1088/1475-7516/2025/07/028](https://doi.org/10.1088/1475-7516/2025/07/028)
- Aihara, H., ALSayyad, Y., Ando, M., et al. 2019, *PASJ*, 71, 114, doi: [10.1093/pasj/psz103](https://doi.org/10.1093/pasj/psz103)
- . 2022, *PASJ*, 74, 247, doi: [10.1093/pasj/psab122](https://doi.org/10.1093/pasj/psab122)
- Andrews, M., Artale, M. C., Kumar, A., et al. 2025, *A&A*, 698, A280, doi: [10.1051/0004-6361/202452628](https://doi.org/10.1051/0004-6361/202452628)
- Blaizot, J., Garel, T., Verhamme, A., et al. 2023, *MNRAS*, 523, 3749, doi: [10.1093/mnras/stad1523](https://doi.org/10.1093/mnras/stad1523)
- Casey, C. M., Cooray, A., Capak, P., et al. 2015, *ApJL*, 808, L33, doi: [10.1088/2041-8205/808/2/L33](https://doi.org/10.1088/2041-8205/808/2/L33)
- Chiang, Y.-K., Overzier, R., & Gebhardt, K. 2013, *ApJ*, 779, 127, doi: [10.1088/0004-637X/779/2/127](https://doi.org/10.1088/0004-637X/779/2/127)
- Chiang, Y.-K., Overzier, R. A., Gebhardt, K., & Henriques, B. 2017, *ApJL*, 844, L23, doi: [10.3847/2041-8213/aa7e7b](https://doi.org/10.3847/2041-8213/aa7e7b)
- Cucciati, O., Lemaux, B. C., Zamorani, G., et al. 2018, *A&A*, 619, A49, doi: [10.1051/0004-6361/201833655](https://doi.org/10.1051/0004-6361/201833655)
- DESI Collaboration, Aghamousa, A., Aguilar, J., et al. 2016, arXiv e-prints, arXiv:1611.00037, doi: [10.48550/arXiv.1611.00037](https://doi.org/10.48550/arXiv.1611.00037)
- DESI Collaboration, Abareschi, B., Aguilar, J., et al. 2022, *AJ*, 164, 207, doi: [10.3847/1538-3881/ac882b](https://doi.org/10.3847/1538-3881/ac882b)
- DESI Collaboration, Abdul-Karim, M., Adame, A. G., et al. 2025, arXiv e-prints, arXiv:2503.14745, doi: [10.48550/arXiv.2503.14745](https://doi.org/10.48550/arXiv.2503.14745)
- Dey, A., Lee, K.-S., Reddy, N., et al. 2016, *ApJ*, 823, 11, doi: [10.3847/0004-637X/823/1/11](https://doi.org/10.3847/0004-637X/823/1/11)
- Dey et al., A. e. a. in prep, *DESI Spectroscopy of Lyman Alpha Emitting Galaxy Candidates*
- Erb, D. K., Steidel, C. C., Trainor, R. F., et al. 2014, *ApJ*, 795, 33, doi: [10.1088/0004-637X/795/1/33](https://doi.org/10.1088/0004-637X/795/1/33)
- Firestone, N. M., Gawiser, E., Ramakrishnan, V., et al. 2024, *ApJ*, 974, 217, doi: [10.3847/1538-4357/ad71c9](https://doi.org/10.3847/1538-4357/ad71c9)
- Furusawa, H., Kosugi, G., Akiyama, M., et al. 2008, *ApJS*, 176, 1, doi: [10.1086/527321](https://doi.org/10.1086/527321)
- Guo, Y., Jiang, L., Egami, E., et al. 2020, *ApJ*, 902, 137, doi: [10.3847/1538-4357/abb59a](https://doi.org/10.3847/1538-4357/abb59a)
- Guy, J., Bailey, S., Kremin, A., et al. 2023, *AJ*, 165, 144, doi: [10.3847/1538-3881/acb212](https://doi.org/10.3847/1538-3881/acb212)
- Hashimoto, T., Ouchi, M., Shimasaku, K., et al. 2013, *ApJ*, 765, 70, doi: [10.1088/0004-637X/765/1/70](https://doi.org/10.1088/0004-637X/765/1/70)
- Herrera, D., Gawiser, E., Benda, B., et al. 2025, *ApJL*, 988, L57, doi: [10.3847/2041-8213/adecc82](https://doi.org/10.3847/2041-8213/adecc82)
- Huang, Y., Lee, K.-S., Shi, K., et al. 2021, *ApJ*, 921, 4, doi: [10.3847/1538-4357/ac1acc](https://doi.org/10.3847/1538-4357/ac1acc)
- Huang, Y., Lee, K.-S., Cucciati, O., et al. 2022, *ApJ*, 941, 134, doi: [10.3847/1538-4357/ac9ea4](https://doi.org/10.3847/1538-4357/ac9ea4)
- Im, S. H., Hwang, H. S., Park, J., et al. 2024, *ApJ*, 972, 196, doi: [10.3847/1538-4357/ad67d2](https://doi.org/10.3847/1538-4357/ad67d2)
- Ito, K., Tanaka, M., Valentino, F., et al. 2023, *ApJL*, 945, L9, doi: [10.3847/2041-8213/acb49b](https://doi.org/10.3847/2041-8213/acb49b)
- Jin, S., Sillassen, N. B., Magdis, G. E., et al. 2024, *A&A*, 683, L4, doi: [10.1051/0004-6361/202348540](https://doi.org/10.1051/0004-6361/202348540)
- Lee, K.-S., Gawiser, E., Park, C., et al. 2024, *ApJ*, 962, 36, doi: [10.3847/1538-4357/ad165e](https://doi.org/10.3847/1538-4357/ad165e)
- Lemaux, B. C., Cucciati, O., Le Fèvre, O., et al. 2022, *A&A*, 662, A33, doi: [10.1051/0004-6361/202039346](https://doi.org/10.1051/0004-6361/202039346)
- Liang, Y., Kashikawa, N., Cai, Z., et al. 2021, *ApJ*, 907, 3, doi: [10.3847/1538-4357/abcd93](https://doi.org/10.3847/1538-4357/abcd93)
- Liang, Y., Ouchi, M., Sun, D., et al. 2025, *ApJ*, 986, 60, doi: [10.3847/1538-4357/adc1bb](https://doi.org/10.3847/1538-4357/adc1bb)
- Miller, T. N., Doel, P., Gutierrez, G., et al. 2024, *AJ*, 168, 95, doi: [10.3847/1538-3881/ad45fe](https://doi.org/10.3847/1538-3881/ad45fe)
- Momose, R., Shimasaku, K., Kashikawa, N., et al. 2021, *ApJ*, 909, 117, doi: [10.3847/1538-4357/abd2af](https://doi.org/10.3847/1538-4357/abd2af)
- Moon, B., Yang, Y., Lee, K.-S., et al. 2025, arXiv e-prints, arXiv:2512.17368, doi: [10.48550/arXiv.2512.17368](https://doi.org/10.48550/arXiv.2512.17368)
- Moon, B., Yang, Y., Gawiser, E., et al. 2026, arXiv e-prints, arXiv:2601.01991, doi: [10.48550/arXiv.2601.01991](https://doi.org/10.48550/arXiv.2601.01991)
- Muldrew, S. I., Hatch, N. A., & Cooke, E. A. 2018, *MNRAS*, 473, 2335, doi: [10.1093/mnras/stx2454](https://doi.org/10.1093/mnras/stx2454)
- Nagaraj, G., Ciardullo, R., Gronwall, C., et al. 2025, arXiv e-prints, arXiv:2506.14510, doi: [10.48550/arXiv.2506.14510](https://doi.org/10.48550/arXiv.2506.14510)
- Nanayakkara, T., Glazebrook, K., Schreiber, C., et al. 2025, *ApJ*, 981, 78, doi: [10.3847/1538-4357/ada6ac](https://doi.org/10.3847/1538-4357/ada6ac)
- Nelson, D., Springel, V., Pillepich, A., et al. 2019, *Computational Astrophysics and Cosmology*, 6, 2, doi: [10.1186/s40668-019-0028-x](https://doi.org/10.1186/s40668-019-0028-x)
- Newman, A. B., Rudie, G. C., Blanc, G. A., et al. 2020, *ApJ*, 891, 147, doi: [10.3847/1538-4357/ab75ee](https://doi.org/10.3847/1538-4357/ab75ee)
- Newman, A. B., Qezlou, M., Rudie, G. C., et al. 2025a, *ApJ*, 988, 47, doi: [10.3847/1538-4357/ade0b2](https://doi.org/10.3847/1538-4357/ade0b2)
- Newman, A. B., Chartab, N., Qezlou, M., et al. 2025b, *ApJ*, 988, 48, doi: [10.3847/1538-4357/ade3c3](https://doi.org/10.3847/1538-4357/ade3c3)
- Oteo, I., Ivison, R. J., Dunne, L., et al. 2018, *ApJ*, 856, 72, doi: [10.3847/1538-4357/aaa1f1](https://doi.org/10.3847/1538-4357/aaa1f1)

- Pillepich, A., Springel, V., Nelson, D., et al. 2018a, MNRAS, 473, 4077, doi: [10.1093/mnras/stx2656](https://doi.org/10.1093/mnras/stx2656)
- Pillepich, A., Nelson, D., Hernquist, L., et al. 2018b, MNRAS, 475, 648, doi: [10.1093/mnras/stx3112](https://doi.org/10.1093/mnras/stx3112)
- Pinarski, E., Ramgopal, G., Firestone, N., et al. 2026, arXiv e-prints, arXiv:2603.09905, <https://arxiv.org/abs/2603.09905>
- Popescu, R., Pope, A., Lee, K.-S., et al. 2023, ApJ, 958, 12, doi: [10.3847/1538-4357/acee79](https://doi.org/10.3847/1538-4357/acee79)
- Poppett, C., Tyas, L., Aguilar, J., et al. 2024, AJ, 168, 245, doi: [10.3847/1538-3881/ad76a4](https://doi.org/10.3847/1538-3881/ad76a4)
- Ramakrishnan, V., Moon, B., Im, S. H., et al. 2023, ApJ, 951, 119, doi: [10.3847/1538-4357/acd341](https://doi.org/10.3847/1538-4357/acd341)
- Ramakrishnan, V., Lee, K.-S., Artale, M. C., et al. 2024, arXiv e-prints, arXiv:2406.08645, doi: [10.48550/arXiv.2406.08645](https://doi.org/10.48550/arXiv.2406.08645)
- Ramakrishnan, V., Lee, K.-S., Firestone, N., et al. 2025a, ApJ, 982, 74, doi: [10.3847/1538-4357/adb624](https://doi.org/10.3847/1538-4357/adb624)
- Ramakrishnan, V., Ortiz, A., Moon, B., et al. 2025b, arXiv e-prints, arXiv:2511.11826, <https://arxiv.org/abs/2511.11826>
- Schlafly, E. F., Kirkby, D., Schlegel, D. J., et al. 2023, AJ, 166, 259, doi: [10.3847/1538-3881/ad0832](https://doi.org/10.3847/1538-3881/ad0832)
- Sheth, R. K., & Tormen, G. 1999, MNRAS, 308, 119, doi: [10.1046/j.1365-8711.1999.02692.x](https://doi.org/10.1046/j.1365-8711.1999.02692.x)
- Shi, K., Huang, Y., Lee, K.-S., et al. 2019, ApJ, 879, 9, doi: [10.3847/1538-4357/ab2118](https://doi.org/10.3847/1538-4357/ab2118)
- Shimakawa, R., Kodama, T., Hayashi, M., et al. 2017, MNRAS, 468, L21, doi: [10.1093/mnrasl/slx019](https://doi.org/10.1093/mnrasl/slx019)
- Sobral, D., Matthee, J., Darvish, B., et al. 2018, MNRAS, 477, 2817, doi: [10.1093/mnras/sty782](https://doi.org/10.1093/mnras/sty782)
- Sousbie, T. 2011, Monthly Notices of the Royal Astronomical Society, 414, 350, doi: [10.1111/j.1365-2966.2011.18394.x](https://doi.org/10.1111/j.1365-2966.2011.18394.x)
- Steidel, C. C., Adelberger, K. L., Dickinson, M., et al. 1998, ApJ, 492, 428, doi: [10.1086/305073](https://doi.org/10.1086/305073)
- Steidel, C. C., Adelberger, K. L., Shapley, A. E., et al. 2000, ApJ, 532, 170, doi: [10.1086/308568](https://doi.org/10.1086/308568)
- Toshikawa, J., Uchiyama, H., Kashikawa, N., et al. 2018, PASJ, 70, S12, doi: [10.1093/pasj/psx102](https://doi.org/10.1093/pasj/psx102)
- Toshikawa, J., Wuyts, S., Kashikawa, N., et al. 2024, MNRAS, 527, 6276, doi: [10.1093/mnras/stad3162](https://doi.org/10.1093/mnras/stad3162)
- Tsybakov, A. B. 2009, Introduction to Nonparametric Estimation (Springer), doi: <https://doi.org/10.1007/b13794>
- Umehata, H., Tamura, Y., Kohno, K., et al. 2015, ApJL, 815, L8, doi: [10.1088/2041-8205/815/1/L8](https://doi.org/10.1088/2041-8205/815/1/L8)
- Uzsoy, A. S. M., Dey, A., Raichoor, A., et al. 2025, arXiv e-prints, arXiv:2511.17498, doi: [10.48550/arXiv.2511.17498](https://doi.org/10.48550/arXiv.2511.17498)
- White, M., Raichoor, A., Dey, A., et al. 2024, arXiv e-prints, arXiv:2406.01803, doi: [10.48550/arXiv.2406.01803](https://doi.org/10.48550/arXiv.2406.01803)
- Zabl, J., Freudling, W., Møller, P., et al. 2016, A&A, 590, A66, doi: [10.1051/0004-6361/201526378](https://doi.org/10.1051/0004-6361/201526378)